Magnetic Fields in Cosmological Box Simulations Using SWIFT

Elion, Maarten

Magnetic fields in cosmological box simulations using SWIFT

THESIS

submitted in partial fulfillment of the
requirements for the degree of

MASTER OF SCIENCE
in
PHYSICS

Author :	M. Elion
Student ID :	sXXXXXXX
Supervisor :	N. Shchutskyi
	dr. M. Schaller
Second corrector :	dr. S.P. Patil

Leiden, The Netherlands, March 12, 2025

Magnetic fields in cosmological box simulations using SWIFT

M. Elion

Huygens-Kamerlingh Onnes Laboratory, Leiden University
P.O. Box 9500, 2300 RA Leiden, The Netherlands

March 12, 2025

Abstract

Magnetic fields are everywhere in the universe but their origins are still uncertain. In this research we present a set of stable cosmological box simulations of the magnetic field using the MHD branch of the SWIFT open-source SPH simulation code. We have implemented cooling and stellar feedback into the simulations, as well as run a purely adiabatic simulation. We look into the large-scale structure of the magnetic field and observe magnetic field amplification beyond adiabatic for the cooling simulations, up to values of 10^3 μG for cooling only, and 10^2 μG for cooling and stellar feedback. We discuss the magnetic field profile in halos which we find to be a little higher than observed in our universe. We also present fiducial RM maps of the largest halo in the simulations, with central RM values of ~ 10 rad m^{-2} for the adiabatic halo $\sim 10^3$ rad m^{-2} for the cooling and cooling plus stellar feedback halo. The hope is that this code can be very useful in understanding magnetic fields not only in the low density regimes, but also in the high density clusters, and getting closer to understanding the magnetic seeding mechanisms.

Contents

1 Introduction **7**

2 Magnetohydrodynamics **9**
2.1 Equations of MHD 9
2.2 Adiabatic amplification 10
2.3 Smoothed Particle Magnetohydrodynamics 11
2.3.1 Equations of SPMHD 12
2.3.2 Divergence Cleaning 13
2.3.3 Tensile Instability 15
2.3.4 Artificial Resistivity 16

3 Cosmological Box Simulations **17**
3.1 Simulations with Anti-Symmetric $\nabla \cdot \mathbf{B}$ Operator 18
3.1.1 Adiabatic Simulation 18
3.1.2 Radiative Cooling 25
3.1.3 Solving Explosions 27
3.2 Simulations with Symmetric $\nabla \cdot \mathbf{B}$ Operator 30
3.2.1 Adiabatic Simulation 30
3.2.2 Radiative Cooling 31
3.2.3 Radiative Cooling and Stellar Feedback 38
3.3 Faraday Rotation Measure maps 42
3.4 Varying Initial Magnetic Field 43

4 SPH Operator Tests **47**
4.1 Density Contrasts 47
4.1.1 Varying particle mass 47
4.1.2 Varying inter-particle separation 50
4.2 Operator Inaccuracies 51

4.2.1 Explanation SPH divergence operator erros 52

5 Discussion 57

6 Conclusion 59

Chapter 1

Introduction

Magnetic fields are present everywhere in our universe, from strongly magnetised neutron stars, to stars and planets, to weakly magnetised ICM. It is still unclear how these magnetic fields have formed in large scale structure.

There are currently two main hypotheses on the origin of cosmological magnetic fields, primordial magnetic fields formed during eg. inflation, or magnetic fields seeded from galactic outflows (see eg. Subramanian (2016) for a detailed review on seeding processes). The answer could lie in the low-density filaments and voids of the universe, where the seeding signatures would remain untouched. However, research of these regions is hindered by their low magnetisation. Upper bounds for the magnetic field are in the order of nG (Pshirkov et al., 2016) while lower bounds are placed at around 10^{-7} nG (Neronov and Vovk, 2010). Even for more massive structure, extensive research of the magnetic field is hard. Current estimates for the magnetic field in galaxy cluster centres are at µG levels. (eg. Donnert et al. (2018); Osinga et al. (2022, 2025); Govoni et al. (2017); Guidetti et al. (2010)) The most promising method is measuring the faraday rotation measure, but measurements are limited to rare polarised radio sources behind or in galaxy clusters and nearby galaxy clusters to maximise the cluster angular size. (Rudnick and Owen, 2014) Another method to deduce the magnetic field in cluster uses the observation of synchrotron emission. However, this method depends on relatively uncertain mechanisms, and thus results in uncertain magnetic field estimates. (Govoni and Feretti, 2004)

That is where simulations come into play. Previous simulations have shown promising results in simulating cosmological magnetic fields. (eg. Dolag and Stasyszyn (2009); Dubois and Teyssier (2008); Marinacci et al.

(2015); Domínguez-Fernández et al. (2019); Mtchedlidze et al. (2022)) This project will investigate large scale cosmological magnetic fields using the magnetohydrodynamics (MHD) branch of the smoothed particle hydrodynamics (SPH) solver SWIFT. (Schaller et al., 2024, 2018) Swift has the possibility to add various subgrid models to the simulations, which has not been done before for cosmological smoothed particle magnetohydrodynamics (SPMHD) codes.

In chapter 2, the underlying equations of MHD and SPMHD are briefly described. In chapter 3 the simulation methods and results are discussed. In chapter 4 some weaknesses of SPH methods are demonstrated. In chapter 5 the research project and its results are discussed, as well as some future prospects for research, before concluding in chapter 6

Chapter 2

Magnetohydrodynamics

This chapter will be devoted to describing some of the governing equations in both theoretical magnetohydrodynamics (MHD) and the simulation methods of smoothed particle magnetohydrodynamics (SPMHD). For detailed derivations of the MHD equations or more background information see e.g. Galtier (2016); Kulsrud (2004).

2.1 Equations of MHD

The set of non-ideal MHD equations describe the behaviour of a fluid under influence of a magnetic field, for which the conductivity σ is not approximated as infinite and thus the magnetic diffusivity $\eta = 1/\sigma$ is non-zero. These equations are given by:

$$\frac{\partial \rho}{\partial t} + \nabla \cdot (\rho \boldsymbol{v}) = 0 \tag{2.1}$$

$$\rho \left(\frac{\partial \boldsymbol{v}}{\partial t} + \boldsymbol{v} \cdot \nabla \boldsymbol{v} \right) = -\nabla P + \mathbf{J} \times \mathbf{B} \tag{2.2}$$

$$\frac{\partial \mathbf{B}}{\partial t} = \nabla \times (\boldsymbol{v} \times \mathbf{B}) + \eta \Delta \mathbf{B} \tag{2.3}$$

$$\nabla \cdot \mathbf{B} = 0 \tag{2.4}$$

with ρ the fluid density, $\boldsymbol{v}$ the fluid velocity, P the pressure, $\mathbf{B}$ the magnetic field, $\mathbf{J} = (\nabla \times \mathbf{B})/\mu_0$ the magnetic current and $\eta = 1/\sigma$ the magnetic diffusivity

2.2 Adiabatic amplification

Now let us derive a relation which will be used often as reference point in this project, namely the amplification of the magnetic field through adiabatic collapse for ideal MHD.

First, consider a magnetic tube that is bounded by the magnetic field lines themselves and surfaces S_1 and S_2 at either end. In that way the flux through the sides of the tube is zero since the magnetic field is parallel to them. The total flux Φ through that tube is zero because $\nabla \cdot \mathbf{B} = 0$. The total flux is also given by

$$\Phi = \iint_{S_1} \mathbf{B} \cdot \mathbf{n}_1 \mathrm{d}S + \iint_{S_2} \mathbf{B} \cdot \mathbf{n}_2 \mathrm{d}S \tag{2.5}$$

with $\mathbf{n}_1$, $\mathbf{n}_2$ normal vectors to the surface pointing outwards. When looking at the fluxes through the individual surfaces, thus along $\mathbf{B}$, we get

$$\Phi_1 = -\iint_{S_1} \mathbf{B} \cdot \mathbf{n}_1 \mathrm{d}S \tag{2.6}$$

$$\Phi_2 = \iint_{S_2} \mathbf{B} \cdot \mathbf{n}_2 \mathrm{d}S \tag{2.7}$$

Combined, this gives $\Phi_1 = \Phi_2$ or in other words, the flux through a material surface along a magnetic field line does not change.

Secondly we need the Kelvin's theorem, that states that for any divergence-free vector field $\mathbf{C}$

$$\frac{\mathrm{d}}{\mathrm{d}t} \iint_S \mathbf{C} \cdot \mathrm{d}S = \iint_S \left(\frac{\mathrm{d}C}{\mathrm{d}t} - \nabla \times (\boldsymbol{v} \times \mathbf{C}) \right) \cdot \mathrm{d}S \tag{2.8}$$

Where S is a material surface moving with the fluid, composed of the same particles. In the case of ideal MHD, $\eta = 0$, this means that

$$\frac{\mathrm{d}}{\mathrm{d}t} \iint_S \mathbf{B} \cdot \mathrm{d}S = 0 \tag{2.9}$$

This means that for any material surface moving with the fluid, the magnetic flux is constant, which is called Alfvén's theorem. In other words this means that mass elements move with the magnetic field lines and will stay on them. The magnetic field lines are frozen into the fluid, which is why this is also called flux-freezing. Note that this whole derivation only holds in the limit of ideal MHD.

This result can now be used to derive the amplification of the magnetic field during isotropic adiabatic collapse. Consider a spherical volume element of radius R_1 with magnetic field B_1 that collapses into a sphere of

radius R_2 with magnetic field B_2. The flux through the sphere and the mass of the element is conserved because of flux-freezing. The conservation of flux gives us $R_1^2 B_1 = R_2^2 B_2$, while the conservation of mass gives us $R_1^3 \rho_1 = R_2^3 \rho_2$. Combine these two relations gives the following relation for adiabatic collapse:

$$\frac{B_2}{B_1} = \left(\frac{\rho_2}{\rho_1}\right)^{2/3} \tag{2.10}$$

This $B \propto \rho^{2/3}$ relation will be used often as reference point in the upcoming simulations.

2.3 Smoothed Particle Magnetohydrodynamics

Smoothed particle magnetohydrodynamics uses the SPH principles to evolve the magnetic field alongside all other hydrodynamic properties. As a short recap, every particle has a kernel W, which is normalised, isotropic, has a central gradient of zero, and is described as a function of distance r and smoothing length h. The kernel function is described as

$$W(r,h) = \frac{1}{h^{n_d}} w(r/h) \tag{2.11}$$

where n_d the number of dimensions and $w(r/h)$ describes the kernel shape and is dimensionless. The kernels used have a compact support radius (or cut-off radius) $H = \gamma_K h$, with γ_K kernel dependent, beyond which the kernel is zero.

The number and mass density are then given by:

$$\hat{n}_i = \sum_j W_{ij} \tag{2.12}$$

$$\hat{\rho}_i = \sum_j m_j W_{ij} \tag{2.13}$$

with $\hat{n}_i$, $\hat{\rho}_i$ denoting the number and mass density at particle i, the sum running over neighbours j with masses m_j and the kernel notation $W_{ij} = W(r_{ij}, h_i)$, with $r_{ij} = |\mathbf{r}_i - \mathbf{r}_j|$.

Generally for a quantity $\mathbf{Q}$, basic SPH estimates are:

$$\hat{\mathbf{Q}}_i = \frac{1}{\hat{\rho}_i} \sum_j m_j \mathbf{Q}_j W_{ij} \tag{2.14}$$

$$(\nabla \cdot \hat{\mathbf{Q}})_i = \frac{1}{\hat{\rho}_i} \sum_j m_j \mathbf{Q}_j \cdot \nabla_i W_{ij} \tag{2.15}$$

$$(\nabla \times \hat{\mathbf{Q}})_i = \frac{1}{\hat{\rho}_i} \sum_j m_j \mathbf{Q}_j \times \nabla_i W_{ij} \tag{2.16}$$

Where ∇_i denotes the gradient taken at particle i. However, for the magnetic field, more accurate estimators are used for the derivative estimators. These estimators can be divided into a symmetric and an anti-symmetric operator. These are given by:

$$(\nabla \cdot \mathbf{Q})_i = -\rho_i \sum_j m_j \left[\frac{f_{ij}\mathbf{Q}_i}{\rho_i^2} \cdot \nabla_i W_{ij} + \frac{f_{ji}\mathbf{Q}_j}{\rho_j^2} \cdot \nabla_i W_{ji} \right] \tag{2.17}$$

$$(\nabla \cdot \mathbf{Q})_i = -\frac{1}{\rho_i} \sum_j f_{ij} m_j (\mathbf{Q}_i - \mathbf{Q}_j) \cdot \nabla_i W_{ij} \tag{2.18}$$

where f_{ij} a correction factor for variable smoothing lengths.

2.3.1 Equations of SPMHD

The equations that SWIFT solves for the magnetic field are based on those from Price et al. (2018) and (ignoring terms not used in this research) given by:

$$\frac{\mathrm{d}v^i}{\mathrm{d}t} = -\frac{1}{\rho}\frac{\partial M^{ij}}{\partial x^j} + \alpha^i_{\text{visc}} + \alpha^i_{\text{self-grav}} + f^i_{\text{divB}} \tag{2.19}$$

$$\frac{\mathrm{d}u}{\mathrm{d}t} = -\frac{P}{\rho}(\nabla \cdot \boldsymbol{v}) + \frac{\eta}{\rho} J^2 - \Lambda_{\text{cool}} \tag{2.20}$$

$$\frac{\mathrm{d}}{\mathrm{d}t}\left(\frac{\mathbf{B}}{\rho}\right) = \frac{1}{\rho}\left[(\mathbf{B}\cdot\nabla)\boldsymbol{v} + \eta\Delta\mathbf{B} - \nabla\psi + \mathcal{D}_{\text{diss}}\right] \tag{2.21}$$

$$\frac{\mathrm{d}}{\mathrm{d}t}\left(\frac{\psi}{c_h}\right) = -c_h(\nabla\cdot\mathbf{B}) - \frac{1}{2}\frac{\psi}{c_h}(\nabla\cdot\boldsymbol{v}) - \frac{\psi}{c_h\tau_c} + H\frac{\psi_i}{c_{h,i}} \tag{2.22}$$

where the time derivatives are the Lagrangian derivatives, with the Maxwell stress tensor given by

$$M^{ij} = \left(P + \frac{1}{2}\frac{B^2}{\mu_0}\right)\delta^{ij} - \frac{B^i B^j}{\mu_0} \tag{2.23}$$

α^i_{visc}, $\alpha^i_{\text{self-grav}}$ the viscosity and gravity terms respectively, f^i_{divB} a term compensating the presence of the numerical magnetic field divergence in the Maxwell stress tensor (see section 2.3.3). Λ_{cool} describes the gas cooling. ψ the Dedner scalar field cleaning numerical divergences (see section 2.3.2) and $\mathcal{D}_{\text{diss}}$ an artificial resistivity term (see section 2.3.4). c_h is the fast magnetosonic sound speed, derived from the sound speed and the Alfvén wave speed, and H the Hubble parameter.

These equations are discretised as follows:

$$\begin{aligned}\frac{\mathrm{d}\boldsymbol{v}_i}{\mathrm{d}t} =& -\sum_j m_j \left[\frac{f_{ij}\mathbf{M}_i}{\rho_i^2}\frac{\partial W_{ij}}{\partial \mathbf{x}_i} + \frac{f_{ji}\mathbf{M}_j}{\rho_j^2}\frac{\partial W_{ji}}{\partial \mathbf{x}_i}\right] \\ &+ \boldsymbol{\alpha}_{i,\text{visc}} + \boldsymbol{\alpha}_{i,\text{self-grav}} + \boldsymbol{f}_{i,\text{divB}} \qquad (2.24)\\ \frac{\mathrm{d}}{\mathrm{d}t}\left(\frac{\mathbf{B}}{\rho}\right)_i =& -\frac{1}{\rho_i^2}\sum_j f_{ij} m_j \boldsymbol{v}_{ij}[\mathbf{B}_i \cdot \nabla_i W_{ij}] \\ &- \frac{1}{\rho_i}\langle \nabla\psi\rangle_{i,\text{SPH}} \\ &+ 2\frac{\eta}{\rho_i}\sum_j \frac{m_j}{\rho_j}(\mathbf{B}_i - \mathbf{B}_j)\frac{F_{ij}}{r_{ij}} + \frac{1}{\rho_i}\mathcal{D}_{i,\text{diss}} \qquad (2.25)\\ \frac{\mathrm{d}}{\mathrm{d}t}\left(\frac{\psi}{c_h}\right)_i =& c_{h,i}\langle \nabla\cdot\mathbf{B}\rangle_{i,\text{SPH}} \\ &+ \frac{\psi_i}{2c_{h,i}\rho_i}\sum_j m_j \boldsymbol{v}_{ij}\cdot\nabla_i W_{ij} - \frac{\psi_i}{c_{h,i}\tau_{c,i}} + H\frac{\psi_i}{c_{h,i}} \qquad (2.26)\end{aligned}$$

where F_{ij} is the scalar part of the kernel gradient $\nabla_i W_{ij} = \hat{\mathbf{r}}_{ij} F_{ij}$ and $\boldsymbol{v}_{ij} = \boldsymbol{v}_i - \boldsymbol{v}_j$. The SPH operators for $\nabla\psi$ and $\nabla\cdot\mathbf{B}$ have been unspecified, since both the anti-symmetric and the symmetric operators have been used for them. They do form a conjugate pair, thus when the anti-symmetric operator for $\nabla\cdot\mathbf{B}$ is used, the symmetric operator for $\nabla\psi$ has been used and vice versa.

2.3.2 Divergence Cleaning

A problem that arises in all numerical MHD simulations is the divergence constraint on the magnetic field. In the MHD equations it enters only as an initial condition. This can be seen if we start from the induction equation

and take its divergence:

$$\frac{\mathrm{d}\mathbf{B}}{\mathrm{d}t} = \nabla \times (\boldsymbol{v} \times \mathbf{B}) \tag{2.27}$$

$$\nabla \cdot \frac{\mathrm{d}\mathbf{B}}{\mathrm{d}t} = \frac{\mathrm{d}}{\mathrm{d}t}(\nabla \cdot \mathbf{B}) = 0 \tag{2.28}$$

However, due to numerical resolution limits, it can not be enforced indefinitely. It is not only important to keep the divergence low for correctness of the magnetic field, but also to avoid monopole forces which enter in the SPMHD equations of motions. The reason they enter in the equations of motions is because the force that conserves momentum is given by (Price, 2012):

$$\frac{\mathrm{d}v}{\mathrm{d}t} = \frac{\nabla \cdot \mathbf{M}}{\rho} \equiv -\frac{\nabla P}{\rho} + \frac{(\nabla \times \mathbf{B}) \times \mathbf{B}}{\mu_0 \rho} + \frac{\mathbf{B}\nabla \cdot \mathbf{B}}{\mu_0 \rho} \tag{2.29}$$

where the last term is a kind of monopole term of the magnetic field. When this becomes large, there could be significant unphysical effects in the simulation. There will be more on this monopole force in section 2.3.3. For now, we will focus on how to keep the divergence low.

A solution was first found by Dedner et al. (2002) who introduced a scalar field ψ which enters in the induction equation as:

$$\frac{\mathrm{d}\mathbf{B}}{\mathrm{d}t} = \nabla \times (\boldsymbol{v} \times \mathbf{B}) - \nabla\psi \tag{2.30}$$

and evolves as (Price and Monaghan, 2005):

$$\frac{\mathrm{d}\psi}{\mathrm{d}t} = -c_h^2(\nabla \cdot \mathbf{B}) - \frac{\psi}{\tau} \tag{2.31}$$

Combining these two equations gives gives a damped wave equation for the divergence of the magnetic field:

$$\frac{\partial^2(\nabla \cdot \mathbf{B})}{\partial t^2} - c_h^2\nabla^2(\nabla \cdot \mathbf{B}) + \frac{1}{\tau}\frac{\partial(\nabla \cdot \mathbf{B})}{\partial t} = 0 \tag{2.32}$$

From this, we see that there is a hyperbolic propagation with speed c_h of the divergence due to the first right-hand side term of equation 2.31, and parabolic damping at a timescale τ due to the second right-hand side term. Typically, c_h is set to the fast magnetosonic wave speed, and $\tau \equiv \frac{h}{\sigma c_h}$. This formalism was later extended by Tricco and Price (2012) to prevent instabilities at density jumps and free surfaces. They set up a constraint that the

hyperbolic divergence transport should be energy conserving, with the result that including the parabolic damping term could only remove energy from the system. Their conservative equations read:

$$\frac{\mathrm{d}\psi}{\mathrm{d}t} = -c_h^2(\nabla \cdot \mathbf{B}) - \frac{\psi}{\tau} - \frac{1}{2}\psi(\nabla \cdot \boldsymbol{v}), \tag{2.33}$$

where the time derivative is the Lagrangian time derivative $\mathrm{d}/\mathrm{d}t \equiv \partial/\partial t + \mathbf{v} \cdot \nabla$. This was derived assuming constant wave cleaning speeds, both in space and in time. However, in practice this does not hold, which results in non-conservation of energy. This was solved by Tricco et al. (2016) who proposed the equation:

$$\frac{\mathrm{d}}{\mathrm{d}t}\left(\frac{\psi}{c_h}\right) = -c_h(\nabla \cdot \mathbf{B}) - \frac{1}{\tau}\left(\frac{\psi}{c_h}\right) - \frac{1}{2}\left(\frac{\psi}{c_h}\right)(\nabla \cdot \boldsymbol{v}) \tag{2.34}$$

The equation that is used in SWIFT is eq. 2.34 with the addition of a term accounting for an expanding universe:

$$\frac{\mathrm{d}}{\mathrm{d}t}\left(\frac{\psi}{c_h}\right)_{\text{Hubble}} = H\frac{\psi}{c_h} \tag{2.35}$$

2.3.3 Tensile Instability

In the previous section, we showed that the numerically non-zero divergence of the magnetic field shows up in the equation of motion. Because of this, there is a regime where the equation of motion becomes unstable because the stress becomes negative. This happens when $B^2/(2\mu_0) > P$ (Phillips and Monaghan, 1985). To counteract this instability, the unphysical force term is subtracted in the equations of motion as suggested by Børve et al. (2001) and adapted to variable smoothing lengths by Price (2012). This correction is the following expression:

$$\boldsymbol{f}_{\text{divB},i} = -\hat{\mathbf{B}}_i \sum_j m_j \left[\frac{f_{ij}\mathbf{B}_i \cdot \nabla_i W_{ij}}{\rho_i^2} + \frac{f_{ji}\mathbf{B}_j \cdot \nabla_i W_{ji}}{\rho_j^2}\right] \tag{2.36}$$

If $\hat{\mathbf{B}}_i = \mathbf{B}_i$, this term is equivalent to the monopole term in the equations of motion (Powell et al., 1999), given the discretisation used for $\boldsymbol{f}_{\text{divB},i}$ is the same as the one used for the divergence term in the equation of motion (Price, 2012). However it was shown that $\hat{\mathbf{B}}_i = \mathbf{B}_i$ is not necessary at all times to avoid instabilities, specifically that $\hat{\mathbf{B}}_i = \frac{1}{2}\mathbf{B}_i$ is sufficient. (Børve et al., 2004) They also proposed a scheme in which the correction term goes

to zero when the ratio between the gas pressure and the magnetic pressure $\beta \equiv P/P_B > 1$, i.e. when $B^2/(2\mu_0) < P$. Even though using $\hat{\mathbf{B}}_i = \frac{1}{2}\mathbf{B}_i$ was also found successful by Barnes et al. (2012), there were problematic effects in the blast wave simulations by Tricco and Price (2012) when using $\hat{\mathbf{B}}_i = \hat{\beta}\mathbf{B}_i$, with $\hat{\beta} < 1$ (note that $\hat{\beta}$ is not related to the pressure ratio β mentioned before; $\hat{\beta}$ was used often in the literature and for comparison's sake the same notation is used here). Iwasaki (2015) found that the best choice of $\hat{\beta}$ is different for certain regimes, and that there is not a single optimal value for all cases. In SWIFT, following Price et al. (2018), the following value for $\hat{B}^i$ is used:

$$\hat{\mathbf{B}} = \begin{cases} \mathbf{B} & \text{if } \beta < 2 \\ [(10-\beta)\mathbf{B}]/8 & \text{if } 2 < \beta < 10 \\ 0 & \text{otherwise} \end{cases} \tag{2.37}$$

2.3.4 Artificial Resistivity

To accurately capture shocks, an artificial resistivity has been implemented in SWIFT according to Price et al. (2018):

$$\mathcal{D}_{\text{diss},i} = \frac{\rho_i}{2}\eta_{\text{art}} \sum_j m_j v^B_{\text{sig}} \left[\frac{f_{ij}F_{ij}}{\rho_i^2} + \frac{f_{ji}F_{ji}}{\rho_j^2}\right] \mathbf{B}_{ij} \tag{2.38}$$

with adjustable parameter η_{art} and the signal velocity $v^B_{\text{sig}} = |\boldsymbol{v}_{ij} \times \hat{\mathbf{r}}_{ij}|$. It can be interpreted as a physical resistivity, but with a coefficient that is proportional to the resolution. Price et al. (2018)

Chapter 3

Cosmological Box Simulations

To simulate the evolution of the magnetic field throughout the universe, we set up different cosmological box simulations, using the direct induction scheme in the SWIFT
MHD_canvas branch.[1] (Schaller et al., 2024, 2018) All cosmological boxes were initialised with a glass cube at a redshift of $z = 63$ with sides of 150 cMpc.[2] The particles got an initial Beltrami magnetic field given by:

$$\mathbf{B} = B_0 \left[(\sin kz + \cos ky)\hat{\mathbf{x}} + (\sin kx + \cos kz)\hat{\mathbf{y}} + (\sin ky + \cos kx)\hat{\mathbf{z}} \right] \quad (3.1)$$

where $B_0 = 10^{-6}$ cμG unless otherwise specified, and $k = 2\pi/\lambda$ the wavenumber, with $\lambda = L_{\text{box}}/10$ the wavelength. Note that this field is trivially divergence-free. The reason for this field morphology is two-part. Firstly, Beltrami fields have the property that $\nabla \times \mathbf{A} = k\mathbf{A}$, which means that we are able to use the same initial field, corrected by a prefactor, for an initial vector potential field to use in another branch of SWIFT's MHD implementation where we evolve the vector potential. Also this type of configuration means that there are no magnetic forces applied to the particles initially. The cosmology for all the boxes was a ΛCDM model with $\Omega_{\text{CDM}} = 0.2574$, $\Omega_b = 0.0486$, $\Omega_\Lambda = 0.694$, $\Omega_r = 0$ and $h = 0.681$, the FLAMINGO fiducial cosmology. (Schaye et al., 2023)

At the start of the project, the simulations were executed with an anti-symmetric operator for the magnetic field divergence in the Dedner scalar field evolution. Later we switched to a symmetric operator for reasons explained in section 3.2. A large advancement in SPMHD was that a conjugate pair of operators was to be used for the divergence in the Dedner

[1] The code can be obtained at https://gitlab.cosma.dur.ac.uk/swift/swiftsim

[2] The initial conditions are available at http://virgodb.cosma.dur.ac.uk/swift-webstorage/ICs/MHD_cosmo_box/

field evolution and the gradient of the Dedner field in the induction equation. (Tricco and Price, 2012) Therefore by switching to the symmetric operator for the divergence of the magnetic field, we also switch to the anti-symmetric operator for the gradient of the Dedner field. An overview of the presented simulations and their differences can be found in table 3.1.

Alongside all simulations, the Friends-Of-Friends (FoF) algorithm was run. The FoF algorithm is commonly used to find structure in simulations and is implemented in SWIFT with the linking length and minimal linking size set in the parameter file. It only bases the structure finding on particle coordinates which means the algorithm is a robust but not a very refined one. For the purpose of most of this project, this is more than enough. In section 3.3, another structure finder is used. The reasoning behind that will be left until then.

The FoF algorithm only produces a catalogue of groups with the centre of mass, total mass, and the amount of particles in the group. The virial radius R_{200} is computed by sorting the particles by distance to the FoF centre of mass, calculating the average density $\langle \rho(\leq r_i) \rangle$ at every particle distance, and then setting the virial radius as the maximum particle distance to the centre of mass such that $\langle \rho(\leq r_i) \rangle > 200 \rho_{crit}$. The critical density is calculated from the cosmology. The virial mass is then set to the total mass inside this radius. For the remainder of the research, when talking about the virial radii and masses, these radii and masses are implied, unless explicitly stated otherwise.

For the remainder of this chapter, all quantities will be reported in physical units, unless explicitly stated otherwise.

3.1 Simulations with Anti-Symmetric $\nabla \cdot \mathbf{B}$ Operator

3.1.1 Adiabatic Simulation

Firstly, the adiabatic simulation was run (aso-128-ad), which just included gravity and (magneto-)hydrodynamics. The redshift zero slice can be seen in figure 3.1. The magnetic field follows the density approximately and there is also a smooth velocity field. The error metric is defined as $R_0 = h|\nabla \cdot \mathbf{B}|/B$ if the signal-to-noise ratio of the divergence is larger than 10, and set to zero otherwise. The noise is estimated from the expected SPH gradient error $\mathbf{B} \cdot \nabla_{\text{SPH}} 1$. The error metric in the slice seem large as they reach values up to unity, however, most of the large error regions are in

name	operator	resolution	M_g [10^{10} $M_\odot$]	subgrid models	parameter variations
aso-128-ad	anti-symmetric	2×128^3	1.01	-	-
aso-128-ad-ar	anti-symmetric	2×128^3	1.01	-	AR
aso-128-ec	anti-symmetric	2×128^3	1.01	EAGLE Cooling	-
so-128-ad	symmetric	2×128^3	1.01	-	-
so-128-ec	symmetric	2×128^3	1.01	EAGLE Cooling	-
so-128-ec-ar	symmetric	2×128^3	1.01	EAGLE Cooling	AR
so-128-ec-pr	symmetric	2×128^3	1.01	EAGLE Cooling	PR
so-128-ecsf	symmetric	2×128^3	1.01	EAGLE cooling + stellar feedback	-
so-256-ad	symmetric	2×256^3	0.126	-	-
so-256-ec	symmetric	2×256^3	0.126	EAGLE Cooling	-

Table 3.1: *An overview of the presented simulations highlighted in this thesis. More simulations have been run, but their results are not presented, nor used in any of the conclusions. The columns are (A) the name of the simulation, (B) the divergence operator used in the Dedner scalar field evolution, (C) the amount of particles $N = N_{\text{gas}} + N_{\text{DM}}$, (D) the mean gas particle mass, (E) the subgrid models used, and (F) the variations in the parameters of the simulation, with AR meaning a non-zero artificial resistivity, PR a non-zero physical resistivity. The resolution of simulations will often be mentioned without the factor 2 in front.*

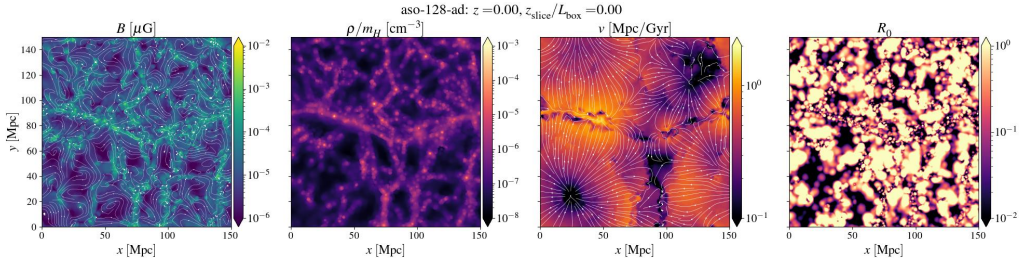

Figure 3.1: *A redshift zero slice of the aso-128-ad simulation. From left to right, the magnetic field, the density, velocity and error metric R_0. For the magnetic and velocity field, the vector field is overlaid on the intensity plot.*

lower density regions. In these regions there are very few particles, so larger smoothing lengths and the error regions seem very large. However, another important sign these errors are acceptable, is that we are not seeing any unphysical large-scale effects.

In the lower left corner of the slices there is a large void. There the initial magnetic field configuration is still visible. Note also that this is such a large void, that there should be almost no magnetisation of this void due to physical processes (that are not present in this particular simulation) in the higher density regions of the simulation, such as AGN heating, stellar feedback or other magnetised jets.

In figure 3.2 the correlation between the magnetic field strength and the gas density can be seen. The simulation follows the adiabatic collapse line neatly. Values of $10^{-2} - 10^{-1}$ μG are reached, which are lower than the

values of order µG typically reached in galaxy cluster centres, but in line with what other adiabatic simulations have found. (Marinacci et al., 2015; Domínguez-Fernández et al., 2019). Note that this simulation corresponds to the box-512.high done by Marinacci et al. (2015) and that our initial magnetic field value is 10^2 lower than the simulation done by Domínguez-Fernández et al. (2019). Also visible is the decrease of the magnetic field in the low density regions, which is in line with the cosmic expansion $\mathbf{B} \propto \mathbf{B}_0/a^2$ that is the dominant effect in these regions.

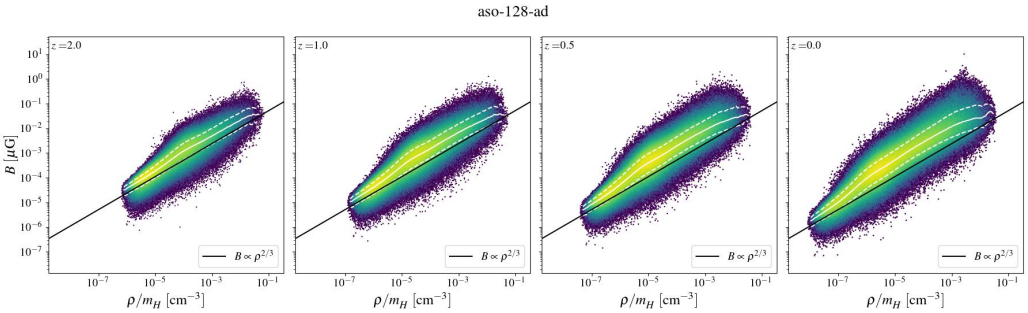

Figure 3.2: *The correlation between the magnetic field and the gas density for the aso-128-ad simulation at redshifts 2, 1, 0.5 and 0. The colour brightness represents the amount of particles in that regime, with brighter colours meaning more particles. In white the percentiles of the distribution are plotted (dashed lines are the 16th and 84th percentile, the solid line the 50th percentile). Also plotted is the $B \propto \rho^{2/3}$ line derived from the flux freezing argument in section 2.2. Note that the height of this line is not exactly calculated, and that the line should be used to compare the slope of the distribution to. The height of the line is set constant throughout this paper*

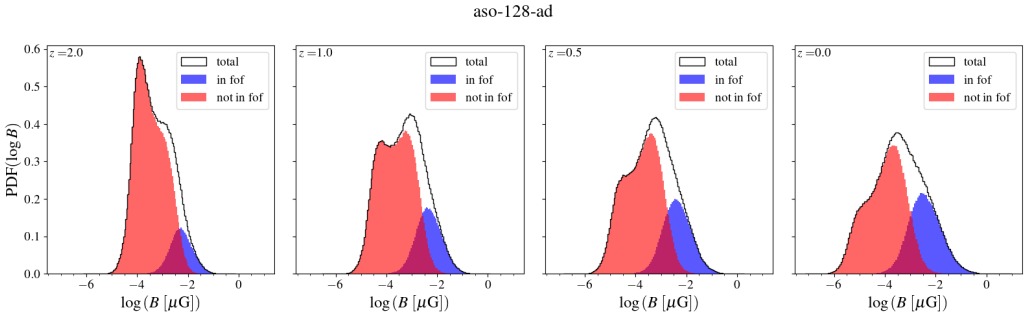

Figure 3.3: *Distribution of the magnetic field strength for redshifts 2, 1, 0.5, 0. In red the magnetic fields of particles not in an FoF group, and in blue the particles that are in an FoF group. In black, the total distribution is shown.*

Version of March 12, 2025– Created March 12, 2025 - 17:00

The distribution of the magnetic field strength can be seen in figure 3.3. A distinction is made between particles in an FoF group and those not in an FoF group. Visible in the figure is the distribution of the non-FoF magnetic fields shifting towards lower magnetic field values, and the distribution of the FoF magnetic fields shifting towards higher values. This is due to the cosmic expansion dominating in the lower density regions, which are mostly not containing FoF groups, and the structure collapse in FoF groups leading to amplification of the magnetic field. Also visible is the total size of the FoF group increasing with lower redshift, which is due to the structure collapse or in other words more particles getting bound.

In figure 3.4 a stacked magnetic field profile is shown of all the FoF halos in the aso-128-ad simulation. The central magnetic fields are at the order of 10^{-2} µG, which is again lower than current observations of galaxy clusters, but in line with other adiabatic galaxy cluster simulations. The profile decreases to $\sim 10^{-3}$ µG at the outskirts of the cluster. Noticeable is a spike in magnetic field at the outskirts of the FoF groups. Firstly, this is an amplified effect of the fact that there are less particles at the outskirts so jumps are more easily made, and second, this can be due to substructure forming in some of the halos.

A closer look at the three most massive FoF halos in the simulation is shown in figure 3.5. This figure shows projections of the clusters instead of slices to better visualise all possible substructure of the cluster, instead of only the substructure present in the slice plane. We can see that the magnetic field is very tangled and random in the cluster centres, as opposed to what was seen in the empty region of the simulated box. There is visible substructure in the density plots, although the density peaks do not correspond to clear peaks in the magnetic field projections. At this point, I would also like to expand on an earlier statement made about the divergence errors in the simulation. When looking at the projected error metric R_0 for the clusters, it can be seen that the error is low in the cluster centre, but increases in the outskirts. This is due to resolution effects, more particles in the centre as opposed to in the outskirts. Therefore these errors in low density regions are very hard to avoid and thus accepted for these simulations.

This same adiabatic run was performed with artificial resistivity turned on, aso-128-ad-ar. The slices can be seen in figure 3.6. Compared to the simulation without artificial resistivity, the errors look much better. Mostly, the errors are lower than 1%. However, the problems with the artificial resistivity run, become clear from the correlation between the magnetic field strength and the density, 3.7. The magnetic field is suppressed by an order of magnitude in the high density regions. Because of this unphysical

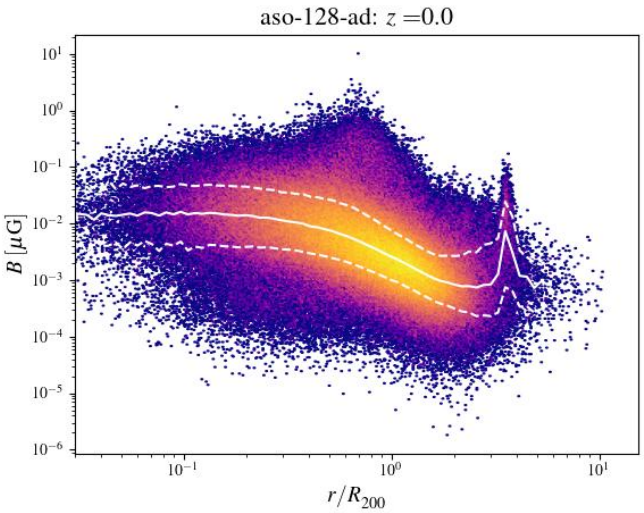

Figure 3.4: *The stacked magnetic field profile of all FoF haloes in the aso-128-ad simulation, at $z = 0$. The distances have been normalized by the virial radii. The colour brightness represents the amount of particles in that regime, with brighter colours meaning more particles. In white the percentiles of the distribution have been plotted, the dashed line representing the 16th and 84th percentiles and the solid line the 50th percentile. Only FoF halos with a virial radius $R_{200} > 0.1$ Mpc have been taken into account.*

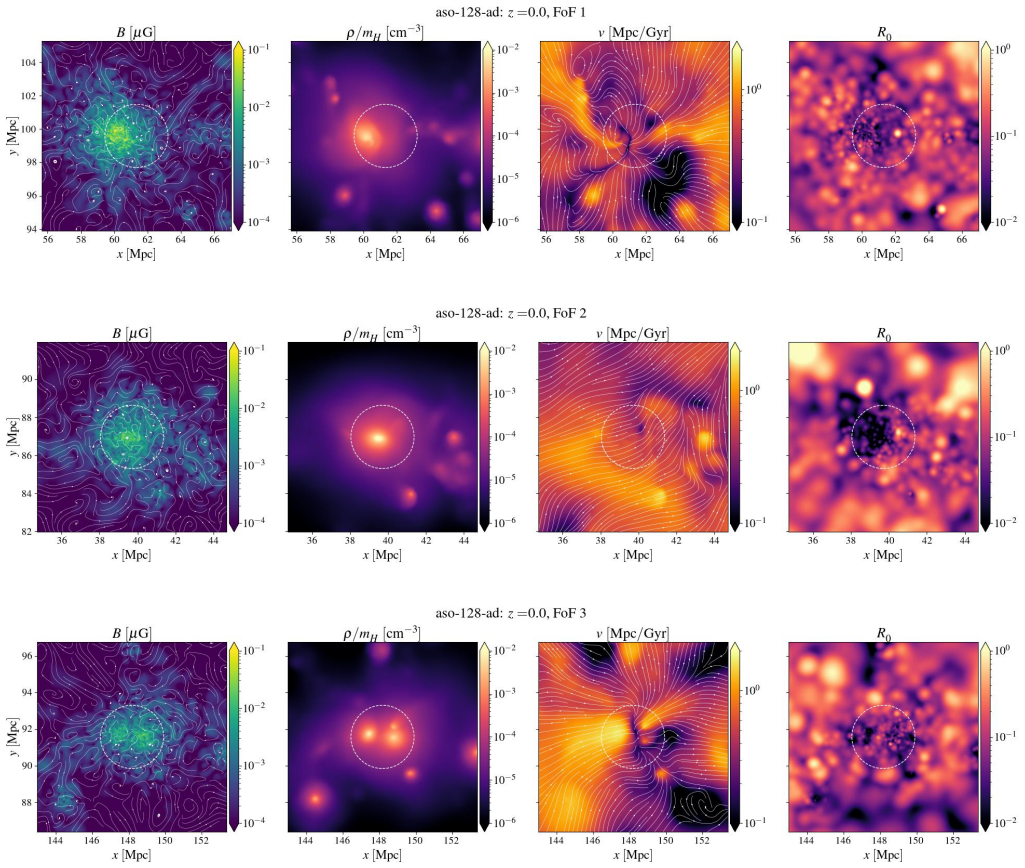

Figure 3.5: *Projections of the three most massive FoF groups in the aso-128-ad simulation sorted by mass from top to bottom, at redshift zero. From left to right, the magnetic field strength with the vector field overlaid, the density, the velocity with the vector field overlaid, and the error metric R_0. The colour scales are the same for every FoF group for comparison's sake. The dashed white circle represents a circle with radius R_200 around the centre of mass of the halo. The illustrated region is $3R_{200}$ for all shown FoF halos. Note that for FoF halo 3, the x coordinates extend to over 150 Mpc, the box size. This is because the halo is positioned at the edge and the box is periodic, thus this is merely a mechanism to plot the whole halo.*

behaviour, no further analysis is done on this simulation.

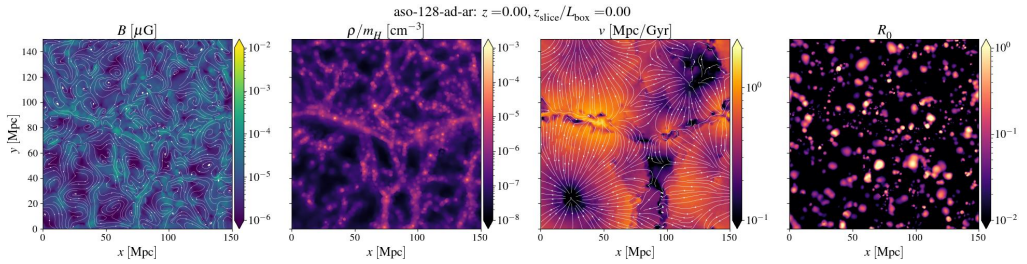

Figure 3.6: *A redshift zero slice of the aso-128-ad-ar simulation. The quantities plotted are the same as figure 3.1.*

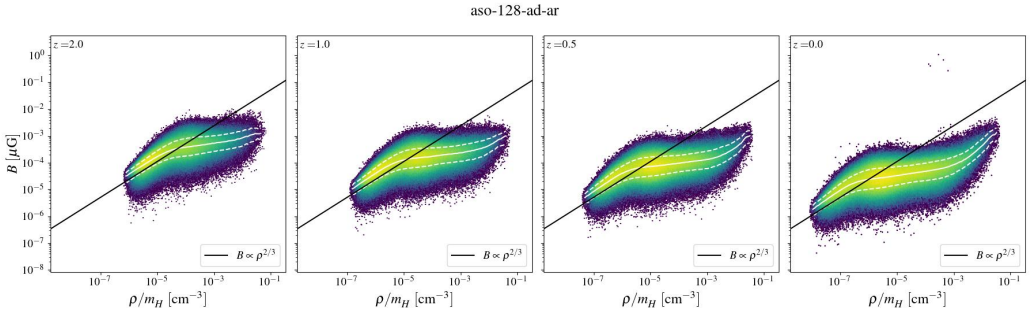

Figure 3.7: *The correlation between the magnetic field and the gas density for the aso-128-ad simulation at redshifts 2, 1, 0.5 and 0. The figure quantities and labels are the same as figure 3.2.*

3.1.2 Radiative Cooling

The next step was adding a cooling model to the simulations, aso-128-ec. We chose to use the EAGLE cooling model and entropy floor, which were already implemented in SWIFT. (Schaye et al., 2015) The cooling rates are based on the tables from Wiersma et al. (2009).[3]

The redshift zero slice of the cooling simulation can be seen in figure 3.8. What immediately stands out, is the fact that there is almost no structure in the magnetic field. Almost the whole box is magnetised, and the magnetic field does not follow the density structure anymore. Also the velocity field is extremely distorted. Also looking at the correlation between the magnetic field strength and the density, fig 3.9(a), we see that the bulk of the particles reside in the low density, high magnetic field strength regime. For some reason, the low density regions got extremely magnetised, up to values of 10^{-1} µG, which is highly unphysical. While for higher densities, one might expect magnetic amplification beyond adiabatic amplification due to shearing motions caused by the cooling, this extra amplification should not be present in the low density regions. (Dubois and Teyssier, 2008)

Now the question is how the particles in low density regions end up highly magnetised. There are two possibilities. One, that the particles in low density regions for some reason "see" or interact with particles in high density regions, or two, that particles from high density regions travel from high density regions to low density regions and magnetise the low density region. Both answers would be wrong in a numerical or physical sense, and should be addressed. The first is wrong in the SPH sense that the particles in low density regions, should not be able to have interactions or neighbours in the high density regions, while the second is wrong in the physical sense that particles from highly bound regions should not be able to escape that easily. To answer what is happening, the particles are tracked throughout the (B, ρ) diagram, see figure 3.9(b). This figure (in comoving units) shows the mean flow of the particles in this diagram. While there are certainly some particles that get magnetised without moving to higher density regions, there is a very clear flow of particles from high density and high magnetic field strength regions towards low density and high magnetic field strength regions. This leads us to suspect the latter of the two hypotheses is the one explaining our problem.

To confirm that there are particles leaving high density regions, we look

[3] For a more rigorous explanation on the implementation of this model in SWIFT, I refer the reader to the SWIFT documentation `https://swift.strw.leidenuniv.nl/docs/SubgridModels/EAGLE/index.html#gas-cooling-wiersma-2009a`

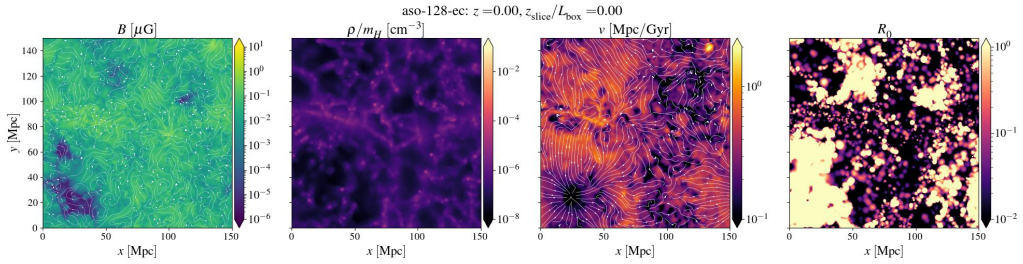

Figure 3.8: *A redshift zero slice of the aso-128-ad-ec simulation. The quantities plotted are the same for figure 3.1.*

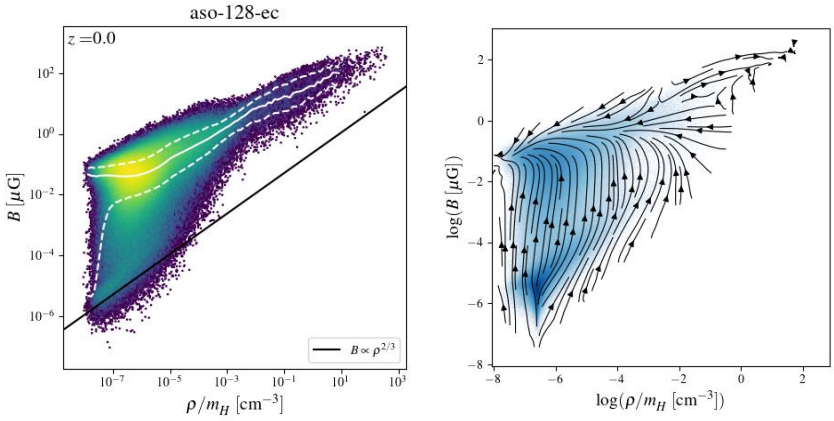

(a) (b)

Figure 3.9: *3.9(a) The correlation between the magnetic field and the gas density for the so-128-ec at redshift zero. The figure quantities and labels are the same as figure 3.2. 3.9(b) The mean motion of the particles through the (B, ρ) space in comoving units. The colouring represents the density of tracks*

into earlier snapshots to see if there are some clues as to what is happening. In figure 3.10 slices of the magnetic field, ratio of magnetic energy to kinetic energy, ratio of magnetic field strength to the density and the velocity are presented. There are multiple regions where all these quantities are high. We identify these regions as explosions that magnetise the surrounding regions. Over time these explosions seem to fill the whole box, leading to the image in figure 3.8. Looking at the particles involved in the explosions, we see that there are quite some particles that get into FoF groups and also very close to the centre (within 10^{-1} Mpc), get high magnetic fields while in the FoF groups, and then leave the groups, while keeping a highly amplified magnetic field. This further supports the hypothesis that magnetisation is due to particles flowing from high to low density regions, which in turn is caused by the observed explosions.

3.1.3 Solving Explosions

The question that in turn needs answering, is why these explosions happen and what there is to be done to prevent them. Something that SPH generally struggles with, is accurately computing quantities, such as divergences, along large density contrasts.[4] Already in an adiabatic simulation there will be large density contrasts between voids, filaments and clusters, but these contrasts will be further amplified when cooling is implemented. Therefore, we first tried adding EAGLE star formation to the cooling model. The hope was that, by turning high density regions into stars, the density contrasts would be less extreme and the SPH operators would be functioning better. However this was not enough to prevent the explosions.

Another attempt to solve the explosions was to turn on artificial resistivity (aso-128-ec-ar), which could help by diffusing the magnetic field from high density regions to prevent a high build-up of magnetic field. Remember, that when the magnetic pressure exceeds the thermal pressure, there is tensile instability, which should be corrected by the Powell term in the SPMHD equations, but could possibly not be enough. While adding artificial resistivity had a large effect on the simulation, the resulting velocity fields were very disturbed unrealistic.

When looking at the individual explosions over redshift (another simulation was done with the same configuration and parameters as aso-128-ec, but with a lot more snapshots over time), one thing that was noticed was that there seemed to be monopole forces acting, defined as forces in

[4] for an analysis on divergence estimation errors at density contrasts, see section 4.1

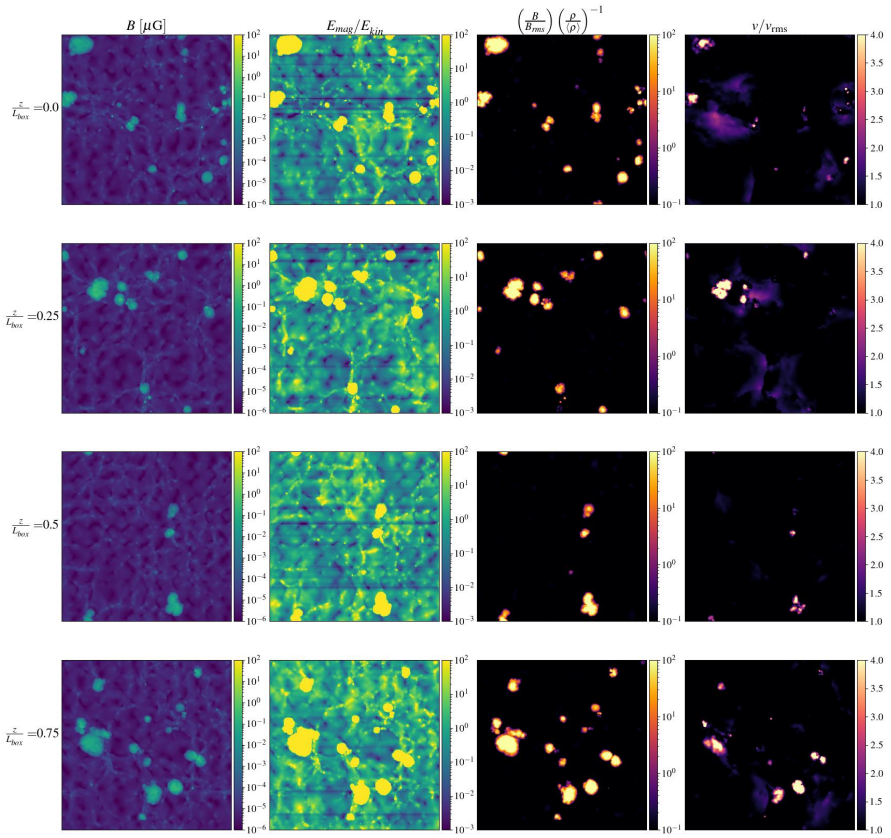

Figure 3.10: *Slices of the aso-128-ec simulation at redshift $z = 4$ at relative slice heights of 0, 0.25, 0.5 and 0.75. The slices from left to right show the magnetic field strength, the ratio of magnetic to kinetic energy, the ratio of the magnetic field strength (in units of root-mean-square magnetic field strength) to the density (in units of average density) to the power two-thirds, and the velocity in terms of root-mean-square velocity. Note that the magnetic field is in comoving units. For the selection of particles based on this quantity it does not matter whether it is in physical or comoving units, since the selection threshold will just move along with the conversion to physical units.*

the direction of $\mathbf{B}(\nabla \cdot \mathbf{B})$. This lead us to believe that the divergence of the magnetic field was a key factor in the problem.

First we tried to tweak the Dedner parameters, to see if we could better clean the divergence. We tried increasing the parabolic Dedner term, to see if this worked in dampening the divergence better, but that did not work. Another thought was to set the hyperbolic parameter to zero, so that divergences were only dampened, but not pushed outwards to other regions. However, the Dedner scalar field is sourced from the hyperbolic part, so without that there is no Dedner scalar field.

Turning off monopole subtraction, eg. not correcting for monopole terms in the equation of motion, seemed to solve the explosions. However this simulation is now wrong for another reason, namely that there are unphysical forces at work, that are not corrected for. This gave rise to the thought that maybe the Powell term is over-correcting the monopole force. To test that hypothesis, we first had to make sure the divergences we were computing were correct. An interesting result in these tests is described in section 4.2. Then we went on to implement a monopole and see if the monopole subtraction term correctly cancelled the monopole force. This was the case, so it was not the monopole subtraction term that was wrongly implemented.

The solution came from one of the PhD students in the MHD group, Orestis Karapiperis. He was trying out the symmetric divergence operator against the anti-symmetric one at density gradients for non-trivially divergence-free magnetic fields. He found that using the anti-symmetric operator, resulted in estimates of the divergence that were closer to zero than when using the symmetric operator. Now the operator that is used in the Powell correction term is the symmetric operator, which stems from the fact that the monopole term in the equation of motion is also symmetric. Now the anti-symmetric divergence operator is used to source the Dedner field. His hypothesis was that the more conservative anti-symmetric divergence operator, was not sourcing the Dedner field enough, leading to under-cleaning of the magnetic divergences. When using a more overestimating operator, the Dedner field would be sourced more, and magnetic divergences could maybe be cleaned better. Trying this version, did indeed prevent the explosions, which will be shown in the next section

3.2 Simulations with Symmetric $\nabla \cdot \mathbf{B}$ Operator

In all simulations presented from this point onwards, the symmetric operator for the magnetic divergence in the Dedner scalar field evolution has been used (as opposed to the anti-symmetric operator), and the anti-symmetric operator for the gradient of the Dedner scalar field in the induction equation (as opposed to the symmetric operator). While the first cosmological tests of this switch were done on the cosmological boxes with cooling, the results presented will be in order of subgrid complexity, thus starting off with the adiabatic runs, followed by the runs with cooling included, and finishing with the run where stellar feedback is implemented as well.

3.2.1 Adiabatic Simulation

For the adiabatic simulations, we have run with two different resolutions, one run with 2×128^3 particles, so-128-ad, and one with 2×256^3 particles, so-256-ad. The same parameters have been used for these runs as their anti-symmetric operator counterpart. In figure 3.11 a slice of both simulations can be seen. For both runs, there is clear structure in the magnetic field, which follows the density structure, and the velocity field is smooth. These quantities are not very different from the previous runs. A large difference from the previous adiabatic simulations is observed in the R_0 slices. While a cautionary note has to be made, namely that these error metrics are now also computed with another operator and they are not one to one comparable, it does seem to be an improvement from the previous runs, since the symmetric divergence operator was mainly overestimating the divergence but still gives lower error metrics. Comparing the two resolutions, there is no big difference except that features in the high-resolution run are a little sharper than for the lower-resolution run, which is to be expected.

The correlation between magnetic field strength and density also behaves very nicely for both resolution runs, see figure 3.12. The 256^3 resolution run has a broader distribution in the diagram, but this is expected for a run with more particles. The magnetic field strength distribution, see figure 3.13 also behaves as expected for both runs, with the particles in FoF groups reaching higher magnetic fields for lower redshifts, and the particles not in FoF groups extending to lower magnetic field strengths due to the cosmic expansion.

In figure 3.14 the stacked magnetic field profiles in both simulations are presented. The profiles are generally decreasing with distance to the

Version of March 12, 2025– Created March 12, 2025 - 17:00

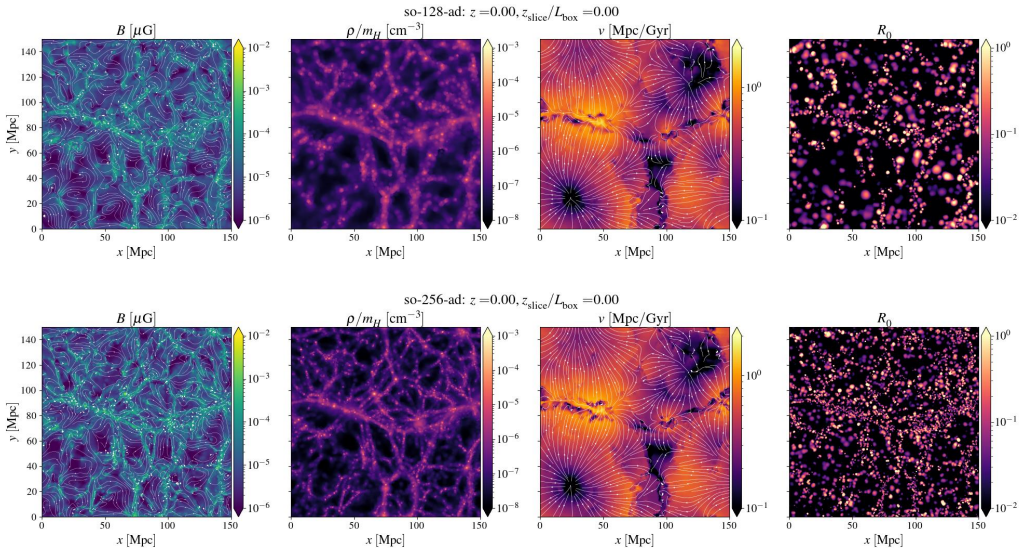

Figure 3.11: *Redshift zero slices of the adiabatic simulations using the symmetric magnetic divergence operator. The quantities plotted are the same as figure 3.1.*

centre, with a central magnetic field strength of $\sim 10^{-2}$ µG for both simulations, although the central magnetic field in the 256^3 simulation is a little higher. Comparing these profiles to the aso-128-ad simulation, there is not a lot of difference. All profiles show some peaks, which could be due to some substructure forming in the FoF halos. This substructure is also visible in the redshift zero projections of the FoF halos, see figure 3.15. In these projections we also see that the central magnetic field is slightly higher for the higher resolution run. We also see more visible substructure in these runs, which is expected from the higher resolution,. The higher the resolution, the smaller the structure one is able to see.

3.2.2 Radiative Cooling

Next, both a 128^3 and a 256^3 resolution simulation was run, but now with the EAGLE Cooling subgrid model implemented in the same way as for the runs with the anti-symmetric operator, section 3.1.2. Redshift zero slices of both simulations are presented in figure 3.16. We see, in contrast to the similar simulations using the anti-symmetric divergence operator, that the magnetic field now follows the density structure and a smooth velocity field. For the 256^3 run, the structure features are sharper, as compared to the 128^3 simulation, but other than that no large differences. Looking at the correlation between the magnetic field and the density in figure 3.17

Version of March 12, 2025– Created March 12, 2025 - 17:00

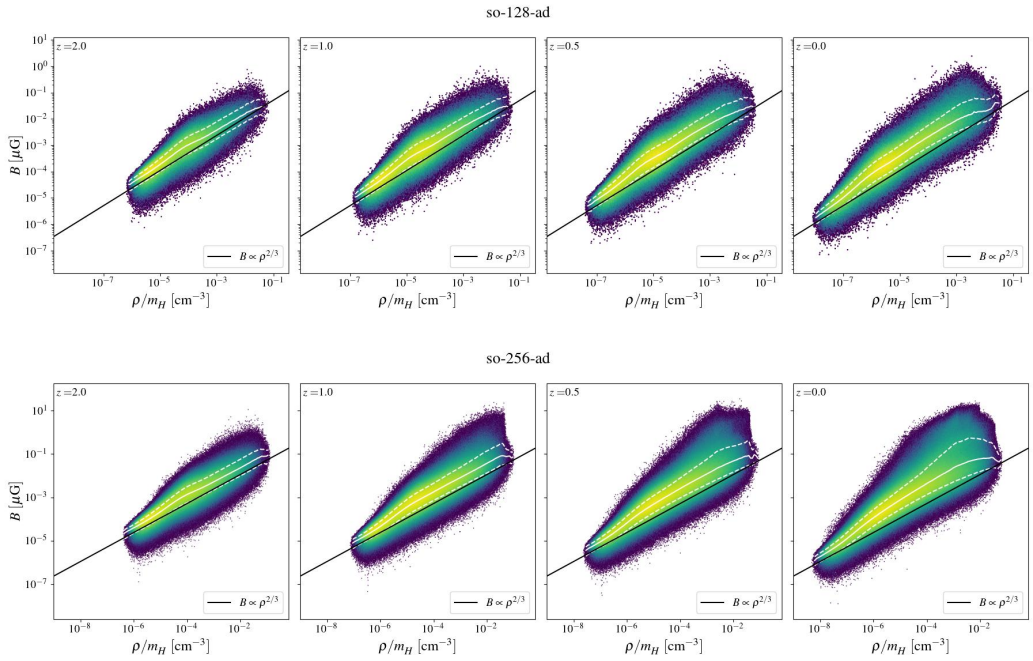

Figure 3.12: *The correlation between the magnetic field and the gas density for the so-128-ad and so-256-ad simulations at redshifts 2, 1, 0.5 and 0. The figure quantities and labels are the same as figure 3.2.*

the stability of using the symmetric divergence operator is shown again. Generally the magnetic field follows the density, with some amplification beyond adiabatic in the mid to high density regime. This amplification beyond adiabatic amplification is expected due to for example shear flows. (Dubois and Teyssier, 2008) Notice also the very large densities reached because of cooling. In runs with other physics implemented, these high densities will not be reached since they would be star forming, and there will be other processes that counteract the collapse into such large densities.

In figure 3.18, the distributions of the magnetic field are presented. Compared to the adiabatic simulations the magnetic field strength has a larger range, and especially the particles in an FoF group are amplified to higher field values. Notice also how the shape of the distribution of particles in FoF has changed to a broader, multi-modal shape. This smearing of the distribution of particles in FoF is also observed by Marinacci et al. (2015). There is a noticeable difference in the shape of the particle distributions in FoF between the two resolution runs. The high magnetic field peak is larger for the high resolution run. However, we do not think this is

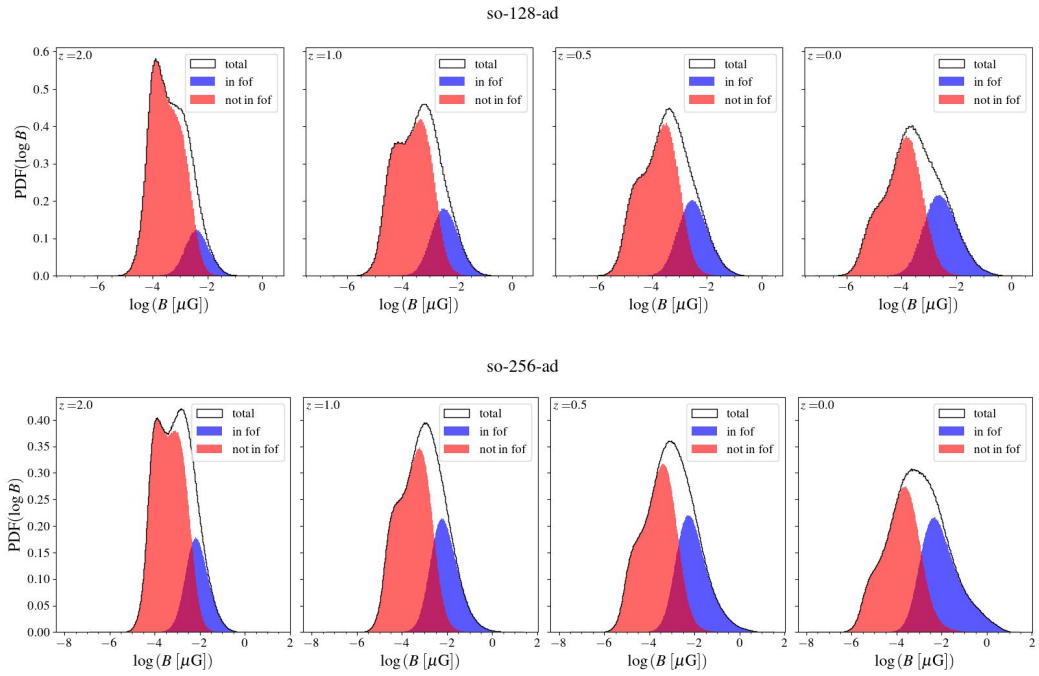

Figure 3.13: *The evolution of the magnetic field strength distribution for the so-128-ad and so-256-ad simulations at redshifts 2, 1, 0.5 and 0. The figure quantities and labels are the same as figure 3.3.*

worrisome since the location of the peaks is roughly the same, and it could then be an effect of the larger particle amount.

Figure 3.19 shows the stacked magnetic field profiles of the FoF halos. Compared to the non-cooling runs, the profiles have a larger central magnetic field, and a steeper decrease in magnetic field strength over distance. The central magnetic field strengths are higher than observed in galaxy clusters, which is not surprising since only cooling has been included here. Also, it is not clear if the magnetic field has saturated in the centres of halos, or if a lower seed field, would result in lower central magnetic fields. Furthermore in real-life galaxy clusters, there are lots of other processes besides cooling that happen at the extremely high densities that are reached in these simulations, which can counteract the density amplification. A very distinct feature in these profiles are these vertical stripes. These are due to the amplified structure collapse because of cooling. Looking at the projections of the FoF halos in figure 3.20, there are distinct peaks in the magnetic field corresponding to peaks in the density projections as well. At first we worried that these peaks might be due to MHD clumping. Looking at projections of a non-MHD run (the same as so-128-ec only

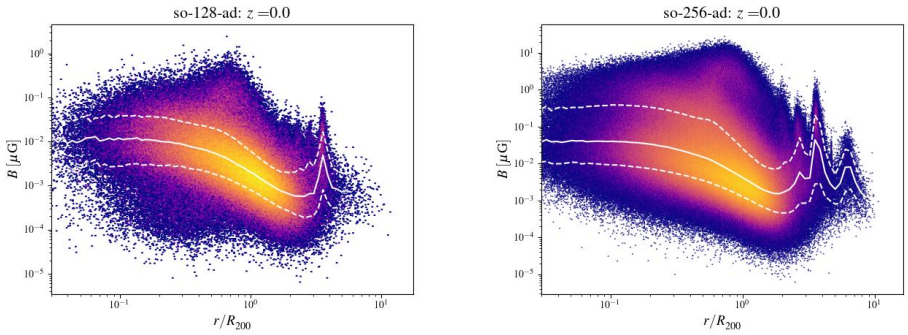

Figure 3.14: *The stacked magnetic field profile of all FoF haloes in the so-128-ad and so-256-ad simulations, at z = 0. The plotted quantities are the same as in figure 3.4.*

without magnetic fields), the density peaks were also observed, thus discrediting that worry.

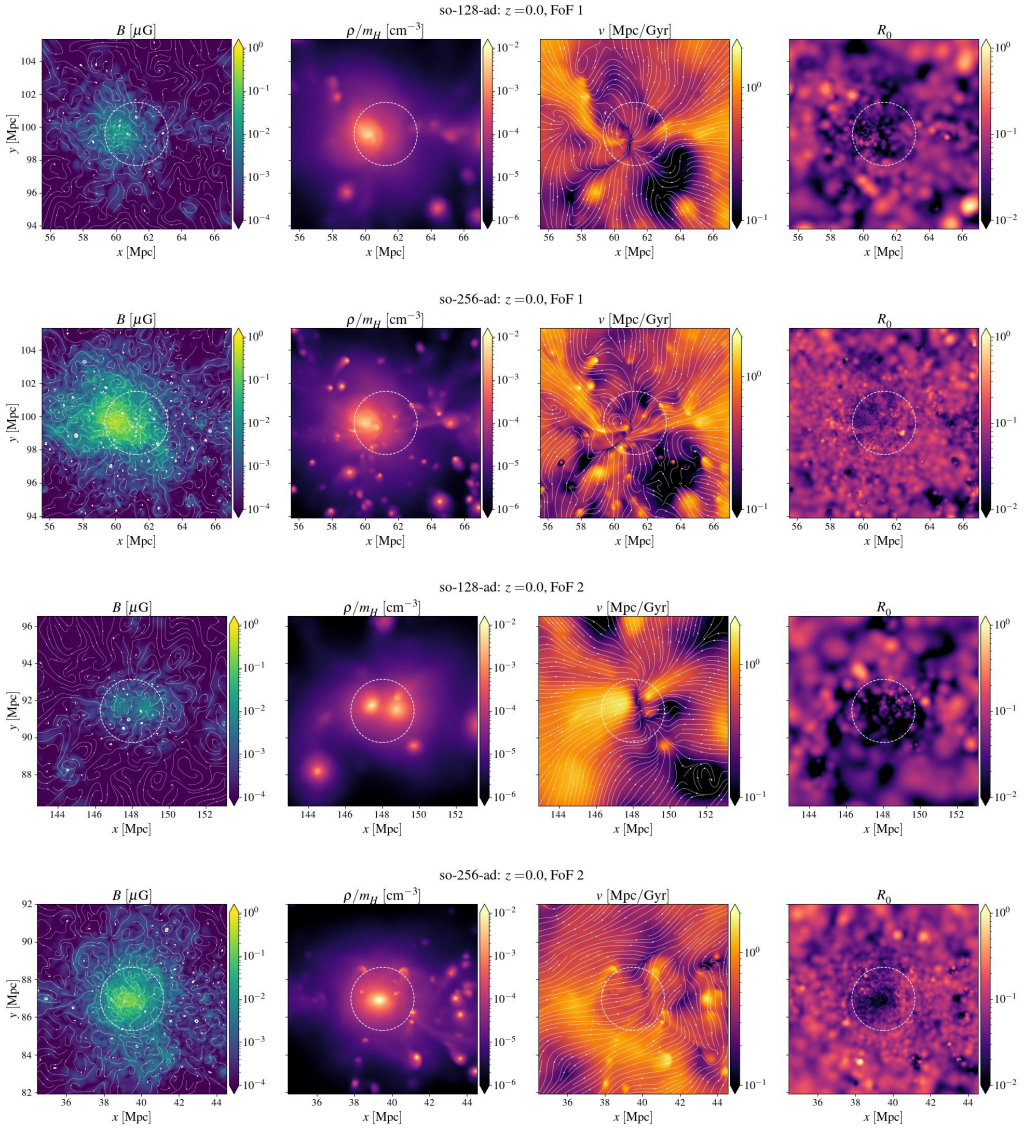

Figure 3.15: *Projections of the two most massive FoF groups in the so-128-ad and so-256-ad simulations, from top to bottom, alternating between so-128-ad and so-256-ad, FoF 1 and FoF 2. The quantities plotted are the same as in figure 3.5.*

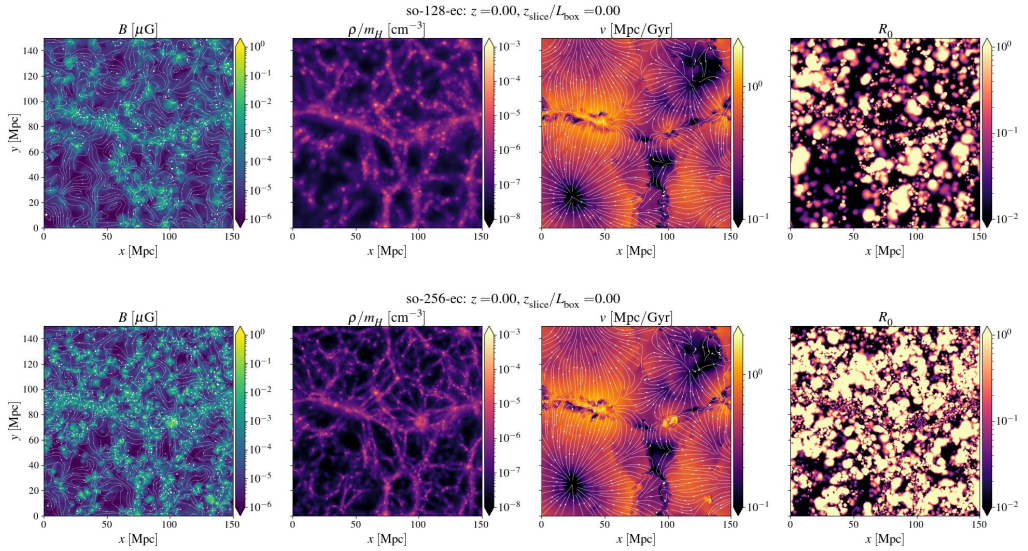

Figure 3.16: *Redshift zero slices of the EAGLE cooling simulations using the symmetric magnetic divergence operator. The quantities plotted are the same as figure 3.1.*

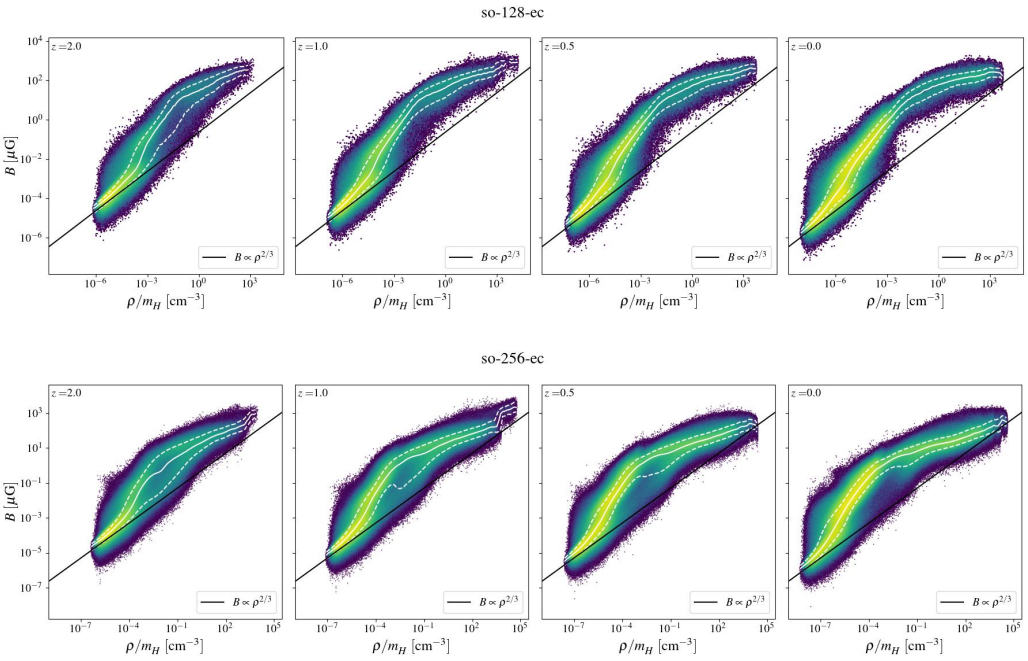

Figure 3.17: *The correlation between the magnetic field and the gas density for the so-128-ec and so-256-ec simulations at redshifts 2, 1, 0.5 and 0. The figure quantities and labels are the same as figure 3.2*

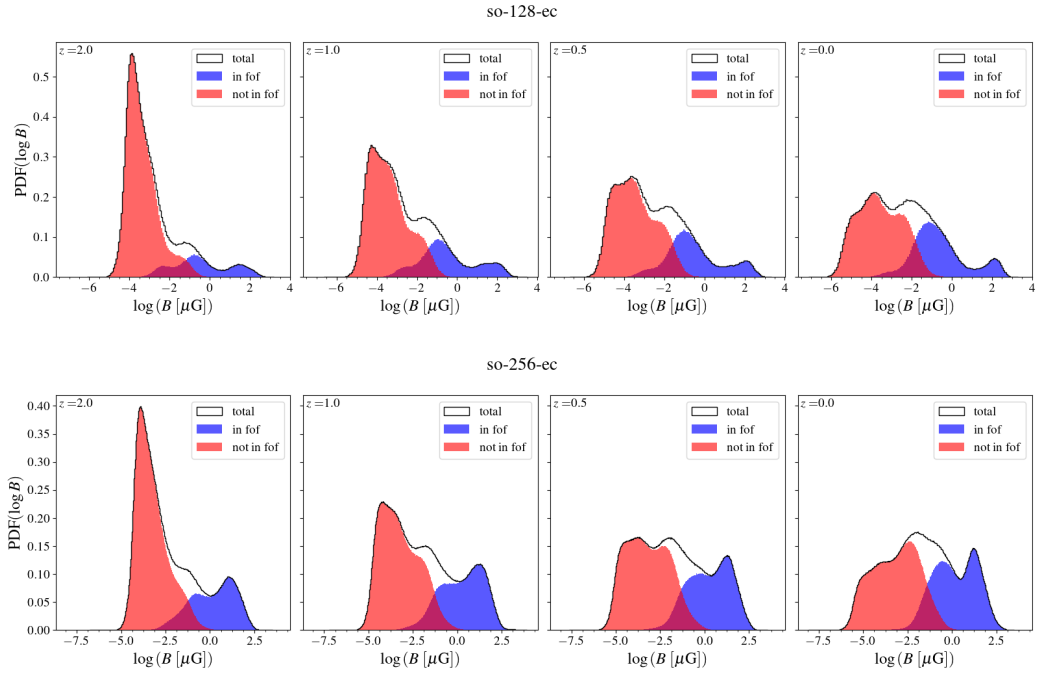

Figure 3.18: *The evolution of the magnetic field strength distribution for the so-128-ec and so-256-ec simulations at redshifts 2, 1, 0.5 and 0. The figure quantities and labels are the same as figure 3.3.*

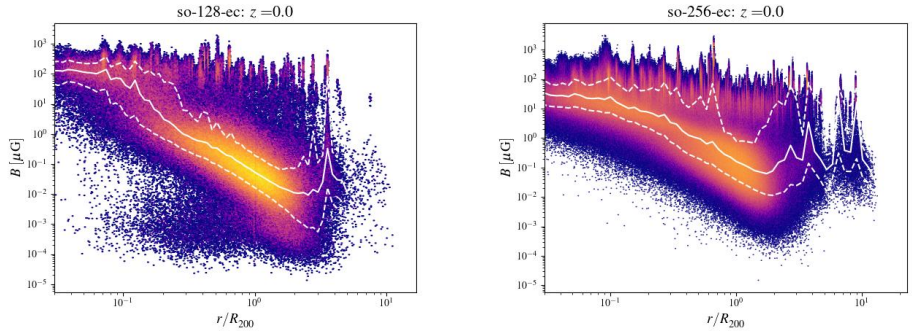

Figure 3.19: *The stacked magnetic field profile of all FoF haloes in the so-128-ec and so-256-ec simulations, at z = 0. The plotted quantities and thresholds are the same as in figure 3.4.*

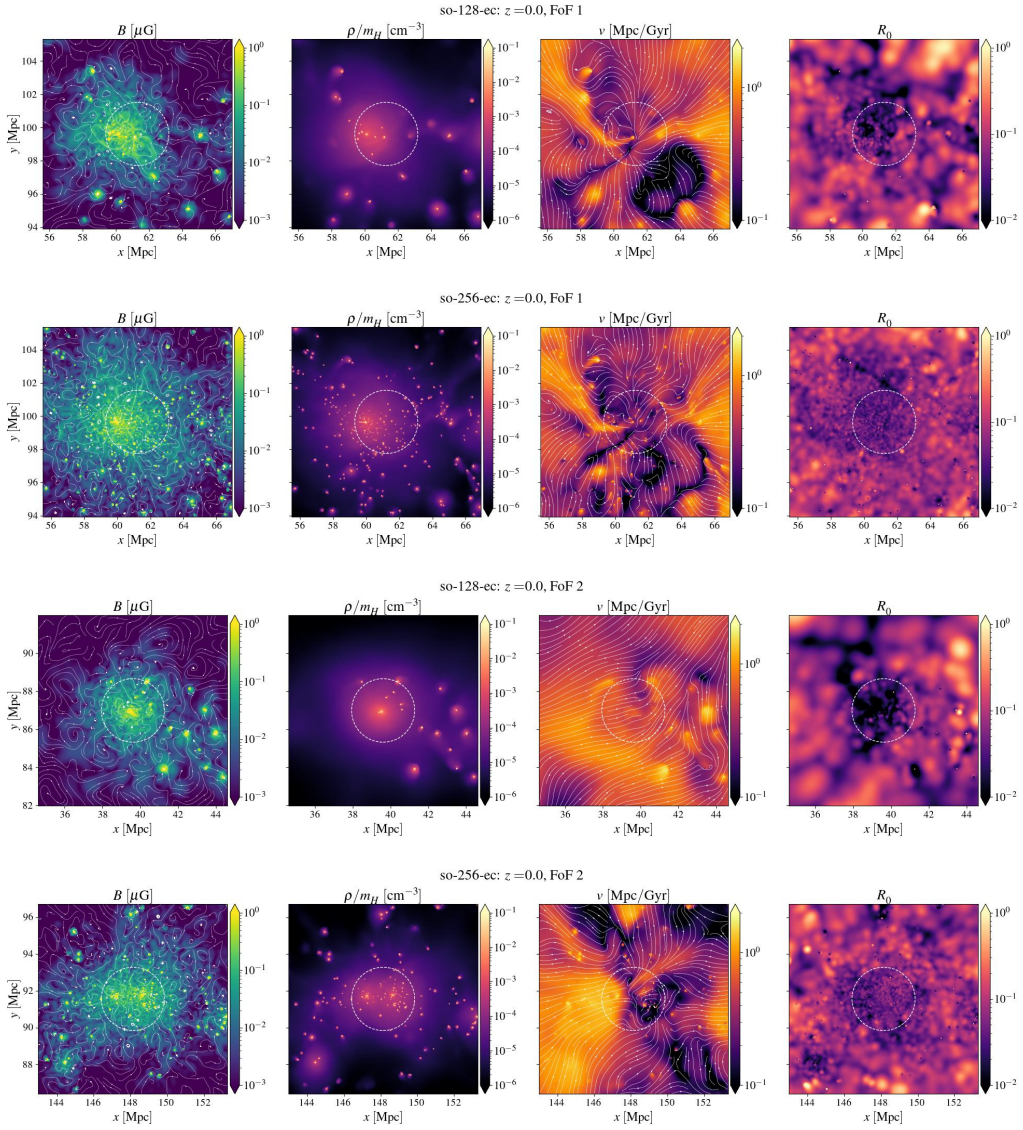

Figure 3.20: *Projections of the two most massive FoF groups in the so-128-ec and so-256-ec simulations, from top to bottom, alternating between so-128-ec and so-256-ec, FoF 1 and FoF 2. The quantities plotted are the same as in figure 3.5.*

3.2.3 Radiative Cooling and Stellar Feedback

Now that we have a stable simulation including cooling, a large question was if adding another subgrid model would make for an unstable simulation. To test that, we included the star formation and stellar feed-

back model from Schaye et al. (2015), simulation so-128-ecsf.[5] We adopt a metallicity dependent density threshold for the star formation, and a pressure law for the star formation rate. The stellar feedback model includes enrichment from AGB stars, SNIa and SNII, and includes energy feedback form SNIa and SNII. The parameters were set to be the same as for the EAGLE simulations. This is not optimal, since it is not tuned to our resolution and particle masses. This means that these simulations would probably not reproduce observed stellar relations well, such as the stellar mass function. (Crain et al., 2015) However, for the purpose of this simulation, namely finding out if the code is stable when this subgrid model is implemented, that is of low priority. Especially since the stellar feedback includes enrichment, which couples non-linearly with the cooling model, the effect this model has on the simulation is non-trivial, and should be tested with the MHD implementation.

Redshift zero slices of the simulation are presented in figure 3.21. The magnetic field follows the density structure, and the velocity field is smooth. Qualitatively, the slices are not much different from the simulation without stellar feedback, also in the error metric. Where the difference from the cooling simulations becomes clear is in the (B, ρ) correlation, see figure 3.22. The gas extends to much lower densities as opposed to the cooling-only simulations, 10 cm^{-3} as opposed to 10^3 cm^{-3}, which is a direct effect of the star formation, which turns high density gas into stars. Also the magnetic field now extends to a little lower values, which goes hand in hand with lower gas densities. The range of magnetic fields presented, also corresponds to earlier findings of Marinacci et al. (2015). The effect of the star formation and feedback model can also be seen in figure 3.23. In that figure we also see the absence of very high density particles in the so-128-ecsf simulation, and see the effect that stellar heating has on star forming regions. Looking at the distribution of the magnetic field, there are almost no differences from the so-128-ec simulation. The difference can be seen in the high-end tail of the FoF-particles, which extends to a little lower values.

The stacked FoF profile is presented in figure 3.25. The vertical peaks all over the profile that were seen for the cooling only simulations are much less visible now. This is expected since the density peaks are converted to star particles. The central magnetic field is about an order of magnitude lower than for its cooling only counterpart, and is now more

[5] For a more rigorous explanation on the implementation of this model in SWIFT, I refer the reader to the SWIFT documentation https://swift.strw.leidenuniv.nl/docs/SubgridModels/EAGLE/index.html#star-formation-schaye-2008-modified-for-eagle

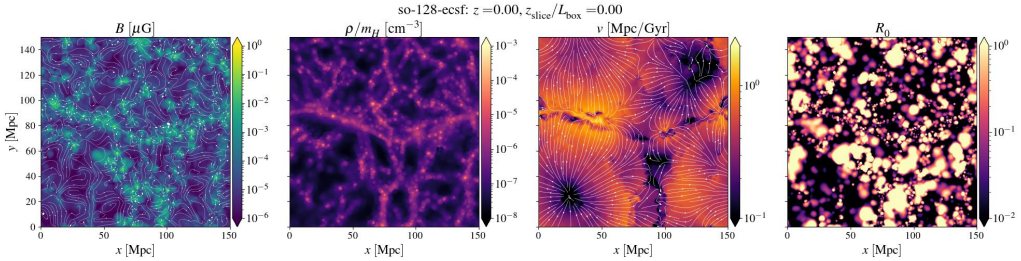

Figure 3.21: *Redshift zero slices of the so-128-ecsf simulation. The quantities plotted are the same as figure 3.1.*

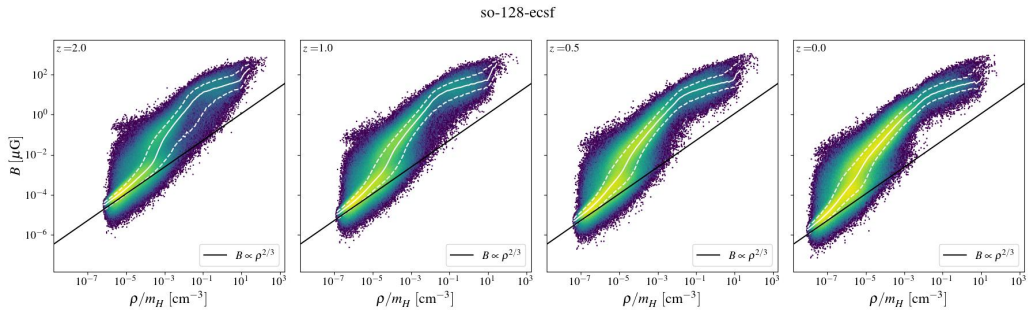

Figure 3.22: *The correlation between the magnetic field and the gas density for the so-128-ecsf simulation at redshifts 2, 1, 0.5 and 0. The figure quantities and labels are the same as figure 3.2.*

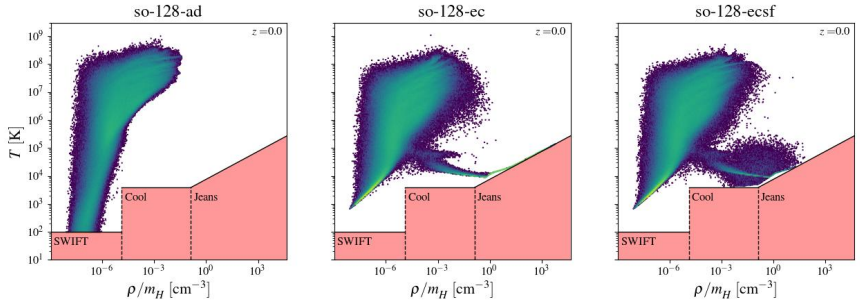

Figure 3.23: *The (T, ρ) diagram of the so-128-ad, so-128-ec and so-128-ecsf simulations. Also plotted are the entropy floors implemented. The "SWIFT" entropy floor is generally used in SWIFT. The "Cool" and "Jeans" entropy floor are floors from the EAGLE entropy floor subgrid model.*

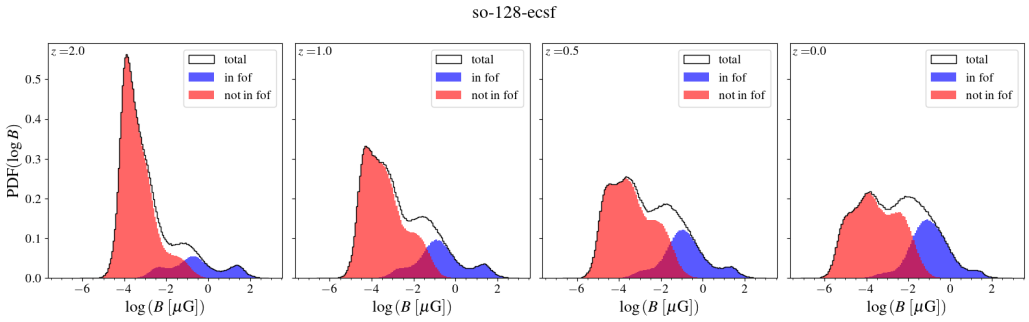

Figure 3.24: *The evolution of the magnetic field strength distribution of the so-128-ecsf simulation at redshifts 2, 1, 0.5 and 0. The figure quantities and labels are the same as figure 3.3.*

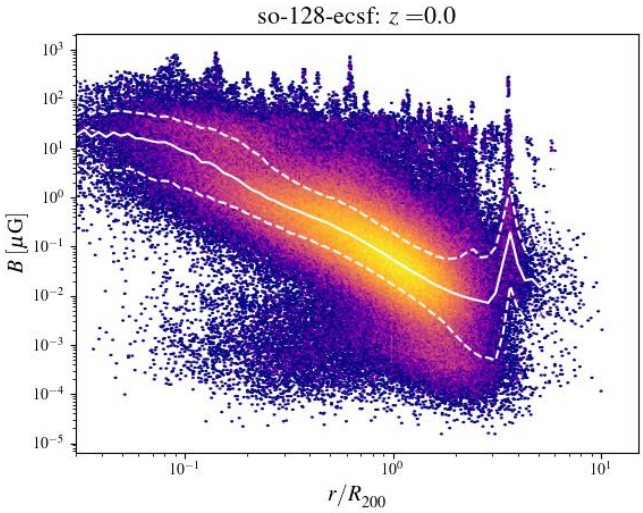

Figure 3.25: *The stacked magnetic field profile of all FoF haloes in the so-128-ecsf simulation, at z = 0. The plotted quantities and thresholds are the same as in figure 3.4.*

in line with (but still on the high end of) observations of cluster centres. The profile extends to lower values of $\sim 10^{-3} - 10^{-2}$ μG at the outskirts of the halo, similar to its cooling only counterpart, and a little higher than its adiabatic counterpart.

3.3 Faraday Rotation Measure maps

One tool researchers use to probe the magnetic field in galaxy clusters, is looking at the polarization of radio sources in the background of clusters. Due to the magnetic fields, the initial polarisation angle Ψ_i will be shifted to the observed polarisation angle Ψ_o according to the relation

$$\Psi_o = \Psi_i + \lambda^2 \mathrm{RM} \tag{3.2}$$

where λ is the wavelength of the radio source, and RM is the faraday rotation measure given by

$$\mathrm{RM} = \frac{e^3}{2\pi m_e^2 c^4} \int_0^L n_e B_{\parallel} \mathrm{d}\ell \tag{3.3}$$

$$\mathrm{RM}\ \left[\frac{\mathrm{rad}}{\mathrm{m}^2}\right] = 812 \int_0^L \left(\frac{n_e}{\mathrm{cm}^3}\right) \left(\frac{B_{\parallel}}{\mu\mathrm{G}}\right) \left(\frac{\mathrm{d}\ell}{\mathrm{kpc}}\right) \tag{3.4}$$

with n_e the electron density, $B_{\parallel}$ the line of sight magnetic field, and the integration goes over the line of sight.(Govoni and Feretti, 2004) Typically the polarisation angle must be observed at a minimum of three wavelengths to lift the $\Psi_o = \Psi_o \pm n\pi$ degeneracy and determine RM accurately.

We have constructed RM maps of the largest halo in the simulations so-128-ad, so-128-ec and so-128-ecsf. Firstly we ran the VELOCIraptor[6] structure finder on all three simulations to get more accurate estimates of the cluster centres, than the robust centre of mass of spatially linked particles that the FoF algorithm gives. (Elahi et al., 2019, 2011) The reason for now using the VELOCIraptor algorithm is that the rotation measure profiles, are very sensitive to the choice of cluster centre, and will not be decreasing over distance if the centre is not at a potential minimum.

To create the RM maps, we take a region of R_{200}, defined with the critical density, around the centre of the most massive halo. The electron density and the magnetic field (line of sight is taken to be in the $\hat{z}$-direction), are projected onto a grid. The integration is performed as a summation in the line-of-sight direction, resulting in the RM maps.

[6]Code is available at https://github.com/pelahi/VELOCIraptor-STF

The naive assumption is made that $n_e = n_H = \rho/m_H$. For diffuse media, this assumption holds reasonably well, but for dense regions it will not. This is because the gas will not be fully ionized or not ionized at all, at very high densities. The electron densities could be computed after completion of the simulations, using the cooling tables, however due to time constraints this was not done.

The rotation measure maps and profiles are presented in figure 3.26. The RM maps are tangled, as expected. We see the values of RM increase with the inclusion of cooling, which leads to higher densities and magnetic fields. The profile of the adiabatic halo has a central value of $|\mathrm{RM}| \sim 20 - 30$ rad m^{-2}. For the halos that include cooling, there was a problem concerning spurious high values of $|\mathrm{RM}|$. These are probably due to the incorrect assumption of electron density, which especially breaks down for high densities in the cluster centre. These spurious values also show up in the average values in the profiles, which is why the median is also included to take care of these spurious outliers. The spurious values are lower when including stellar feedback, which can be explained by the lower gas densities and thus lower discrepancy with the density assumption. Looking at the median profiles of both the so-128-ec and so-128-ecsf simulation, they have a central value of $|\mathrm{RM}| \sim 10^3$ rad m^{-2}. The results of the adiabatic cluster and the cooling clusters correspond with other simulations (Dubois and Teyssier, 2008) and roughly with observations, eg. Guidetti et al. (2008); Govoni et al. (2017) for the adiabatic simulations, and Taylor et al. (2002) for the cooling simulations. The cooling simulations also correspond to the high-end RMs reported in Osinga et al. (2025) The discrepancy between the different observations could be explained by different processes, such as cooling flows, dominating the observed cluster region. One note that also should be made when comparing our presented RM maps to the literature, is that here the most massive halo has been presented with its associated high magnetic field. Thus some bias towards higher RM values is expected. To thoroughly analyse the RM maps, one should also look into the other halos in the simulation.

3.4 Varying Initial Magnetic Field

As a small preview into what studies are possible with the previously presented simulations, we have run a cooling simulation where we started with a different magnetic field configuration. This time, instead of a Beltrami field, the particles get a constant magnetic field of $\mathbf{B}_0 = B_0\hat{x}$ with $B_0 = 10^{-6}$ cμG.

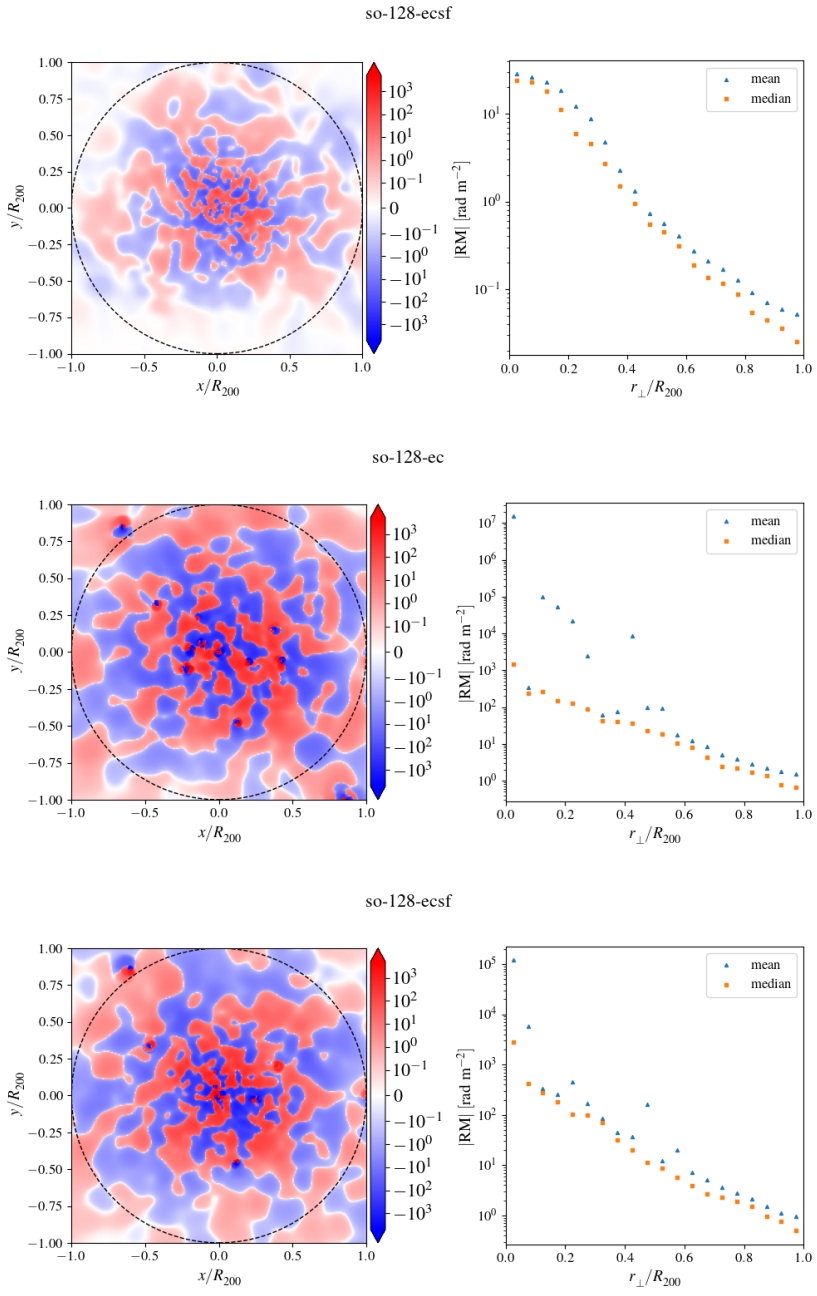

Figure 3.26: *Faraday rotation maps (left) and profiles (right) of the most massive halo in the (top to bottom) so-128-ad, so-128-ec and so-128-ecsf simulations. The profiles are plotted as a function of projected distance from the center, for both the mean and the median. The dashed circle represents the virial radius.*

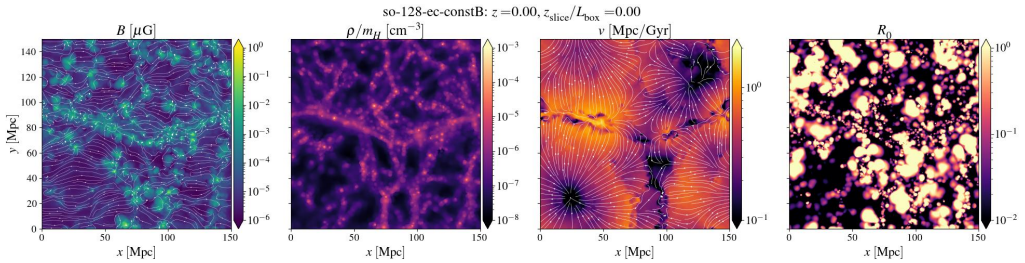

Figure 3.27: *Redshift zero slices of the so-128-ec-constB simulation. The quantities plotted are the same as figure 3.1.*

The redshift zero slices are presented in figure 3.27. We see that in the low density regions the initial magnetic field morphology is still present, as expected. The question that then might be asked, is how much of the initial field morphology is still present in different regions, such as clusters, filaments and voids. Also the effect of the magnetic field on these regions could be investigated. While this research will not go into more depth on this subject, it is a very interesting and promising area of research.

Chapter 4

SPH Operator Tests

4.1 Density Contrasts

A common obstacle in SPH is density contrasts. In this section, the effect of density contrasts on divergence operators will be tested. Two types of density contrasts are constructed. The principle for both of them is a box which is divided into two by different densities over the x direction. For the first type, the constant smoothing length density contrast, the particle masses on the right side are adjusted, and for the second type, the constant mass density contrasts, the inter-particle distance on the right side is adjusted. For both types, there will be a constant magnetic field, resulting in a theoretically zero divergence. Then, the symmetric and the anti-symmetric divergence operators will be tested at these density contrasts.

4.1.1 Varying particle mass

For the first type, we can estimate the resulting divergence at the boundary when using the symmetric divergence operator. This operator is given by:

$$(\nabla \cdot \mathbf{B})_i = -\rho_i \sum_j m_j \left[\frac{f_{ij}\mathbf{B}_i \cdot \nabla_i W_{ij}}{\rho_i^2} + \frac{f_{ji}\mathbf{B}_j \cdot \nabla_i W_{ji}}{\rho_j^2} \right] \tag{4.1}$$

For the test problem, $\mathbf{B}_i = \mathbf{B}_j = \mathbf{B}$, $h_i = h_j = h$ since the particles are on a grid, and thus also $f_{ij} = f_{ji} = 1$. Note this also means that $\nabla_i W_{ij} =$

$\nabla_i W_{ji}$. This gives:

$$(\nabla \cdot \mathbf{B})_i = -\rho_i \mathbf{B} \cdot \sum_j m_j \left[\frac{1}{\rho_i^2} + \frac{1}{\rho_j^2} \right] \nabla_i W_{ij} \tag{4.2}$$

$$= -\frac{\mathbf{B}}{\rho_i} \cdot \sum_j m_j \left[1 + \frac{\rho_i^2}{\rho_j^2} \right] \nabla_i W_{ij} \tag{4.3}$$

At this point, let us look at a particle exactly at the boundary. The neighbours can be divided into neighbours on the left side of the boundary, j_L, and neighbours on the right side of the boundary, j_R. The density at the boundary might be ill-defined, but it will be somewhere in between the two densities, and for the derivation it does not matter what the density actually is. This results in the following equation:

$$(\nabla \cdot \mathbf{B})_i = -\frac{\mathbf{B}}{\rho_i} \cdot \left(\sum_{j_L} m_{j_L} \left[1 + \frac{\rho_i^2}{\rho_{j_L}^2} \right] \nabla_i W_{ij_L} + \sum_{j_R} m_{j_R} \left[1 + \frac{\rho_i^2}{\rho_{j_R}^2} \right] \nabla_i W_{ij_R} \right) \tag{4.4}$$

Now we make some simplifications. First of all, $m_{j_L} = m_L$ and $m_{j_R} = m_R$, following the setup. Second, we make the assumption that the that the step in density at the boundary is direct, thus $\rho_{j_L} = \rho_L$ and $\rho_{j_R} = \rho_R$. This is not exactly true, since with SPH this region will be smoothened a little bit. However, experiments have shown that this almost holds. The last assumption, is that all neighbours can be divided into pairs for which $\nabla W_{ij_L} = -\nabla W_{ij_R}$. This is valid because the particles are placed at a grid and the kernel is anti-symmetric in r/h. With these three assumptions we can modify the equations as follows:

$$(\nabla \cdot \mathbf{B})_i = -\frac{\mathbf{B}}{\rho_i} \cdot \sum_{j_L} \left(m_L \left[1 + \frac{\rho_i^2}{\rho_L^2} \right] \nabla_i W_{ij_L} - m_R \left[1 + \frac{\rho_i^2}{\rho_R^2} \right] \nabla_i W_{ij_L} \right) \tag{4.5}$$

$$= -\frac{\mathbf{B}}{\rho_i} \left(m_L \left[1 + \frac{\rho_i^2}{\rho_L^2} \right] - m_R \left[1 + \frac{\rho_i^2}{\rho_R^2} \right] \right) \cdot \sum_{j_L} \nabla_i W_{ij_L} \tag{4.6}$$

$$= -\frac{m_L}{\rho_i} \mathbf{B} \left(1 - \frac{m_R}{m_L} + \frac{\rho_i^2}{\rho_L^2} \left[1 - \frac{m_L}{m_R} \right] \right) \cdot \sum_{j_L} \nabla_i W_{ij_L} \tag{4.7}$$

This shows that the symmetric divergence operator is not necessarily zero at the boundary for the grid based set-up. Note that it still reduces

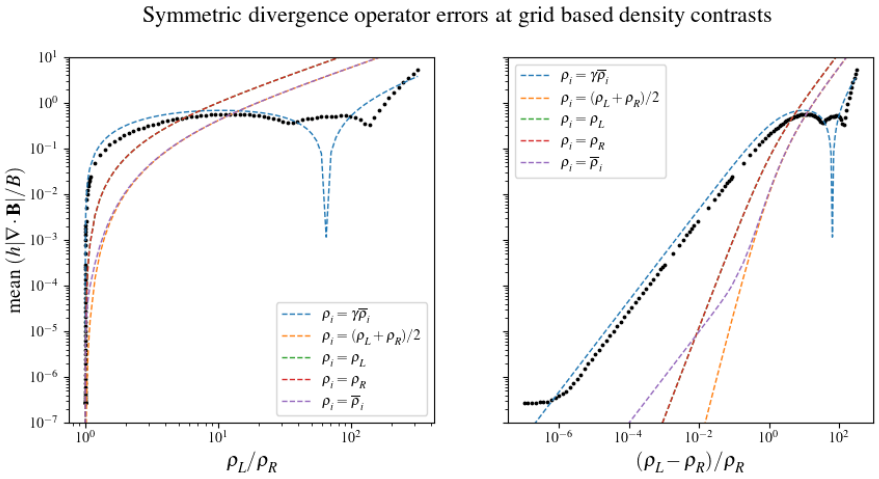

Figure 4.1: *The divergence errors for a grid based density contrast. ρ_L denotes the density on the left side of the box, ρ_R that on the right side. The left figure shows the divergence error as a function of the density ratio, the right the contrast as a function of the relative density difference. The dashed lines represent predictions of the divergence error for different assumptions of ρ_i.*

to zero when there is no density contrast, i.e. $m_L = m_R$, although for real simulations it will be zero to machine precision and not exactly zero.

For the test, a box was set up, filled with 128 particles a side on a grid and a constant magnetic field. The particles in the right half got a lower mass, to create a density contrast. For the divergence error, the mean was taken of the relative divergence error in a thin region around the density jump. This was done for multiple density contrasts. The results can be seen in figure 4.1. This shows that the error in the divergence estimate can become non-negligible at low density contrasts, ie. when the density difference is at the level of 1%. Note that when the density contrast is removed (ie. $\rho_L = \rho_R$), the divergence error is zero to machine precision.

When comparing the results against the derived expected divergence, there is the complication that the density at the boundary is ill-defined. Therefore, we compare it against several assumptions of the density at the boundary: $\rho_i = \gamma\overline{\rho}_i$ (with the special case of $\gamma = 1$ separate, $\rho_i = (\rho_L + \rho_R)/2$, $\rho_i = \rho_L$ and $\rho_i = \rho_R$. We see that a reasonable fit is when $\rho_i = \gamma\overline{\rho}_i$ with $\gamma \approx 0.24$, which mostly underestimates the small bump in the divergence error at high contrasts.

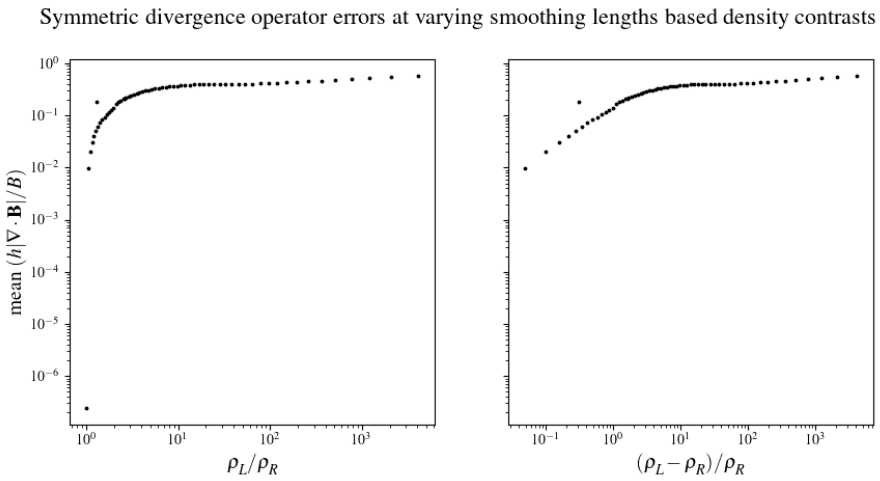

Figure 4.2: *The divergence errors for a varying inter-particle distance based density contrast. ρ_L denotes the density on the left side of the box, ρ_R that on the right side. The left figure shows the divergence error as a function of the density ratio, the right figure the contrast as a function of the relative density difference.*

4.1.2 Varying inter-particle separation

When constructing density contrasts with a varying inter-particle separation, a semi-analytical derivation of the divergence error such as above is much harder, because the f-factors will be non-trivial and the neighbours can not be divided such that they have kernel gradients of equal magnitude, but opposite signs.

The box is set up similar to the test with varying masses, only now N_L particles are placed on the left side of the box, and $N_R \neq N_L$ particles on the right. All particles have the same mass.

In figure 4.2 the divergence error for this set-up is presented. Note that a lot of particles are needed for low density contrasts, and thus the relative contrasts extend less towards lower values than for the previous test. Also here we see that divergence errors pop up for small density contrasts. The errors seem roughly the same, although varying the particle separation seems to saturate at higher contrasts. This saturation is likely due to the fact that the particles at the boundary, will only ”see” particles on the left side, and that configuration will not change when removing particles from the right side. Thus the errors should stabilise at high contrasts. Also note, as a consistency check, that the divergence error disappears when the density contrast is removed.

4.2 Operator Inaccuracies

At one point, the question arose whether the monopole correction term was behaving as it should, or whether it was overcompensating and thus causing explosions. To investigate that, the first question one should ask is if the operators are giving the correct divergence. A small box was set up, filled with particles on a grid with a fiducial magnetic field with a known divergence. The set up used an electric-field-like monopole which was constructed as follows:

$$\mathbf{B} = \mathbf{B}_m + \mathbf{B}_b \tag{4.8}$$

$$\mathbf{B}_m = \begin{cases} B_m \left[\left(\frac{r_s}{r} \right)^2 - 1 \right] \hat{r} & \text{if } r \leq r_s \\ 0 & \text{if } r > r_s \end{cases} \tag{4.9}$$

$$\mathbf{B}_b = B_b \hat{z} \tag{4.10}$$

where $\mathbf{B}$, $\mathbf{B}_m$ and $\mathbf{B}_b$ are the total, monopole and background magnetic fields respectively. r is the distance of the particle to the centre of the monopole, and r_s is the monopole size, i.e. where the monopole field is used. This was implemented to have a region where there should be divergence and a region where the field should be divergence-less. The $1/r^2$ dependence was chosen to resemble an electric field monopole, while the -1 term in the monopole field was used to force a continuous (not differentiable at the boundary) magnetic field. Do note, that this is a very large monopole and a monopole like this should not occur in normal simulations, but for testing the operators themselves it is not of importance.

The divergence of this field can be analytically derived (except at the boundary where the derivative is not continuous) and is given by:

$$\nabla \cdot \mathbf{B} = \nabla \cdot \mathbf{B}_m \tag{4.11}$$

$$= \frac{1}{r^2} \frac{\partial (r^2 B_{m,r})}{\partial r} \tag{4.12}$$

$$= \begin{cases} -B_m \frac{2}{r} & \text{if } r < r_s \\ 0 & \text{if } r > r_s \end{cases} \tag{4.13}$$

The resulting fields are presented for both the anti-symmetric and the symmetric operator in figure 4.3. There is a clear region in the centre of the monopole where SWIFT has computed a wrong divergence.

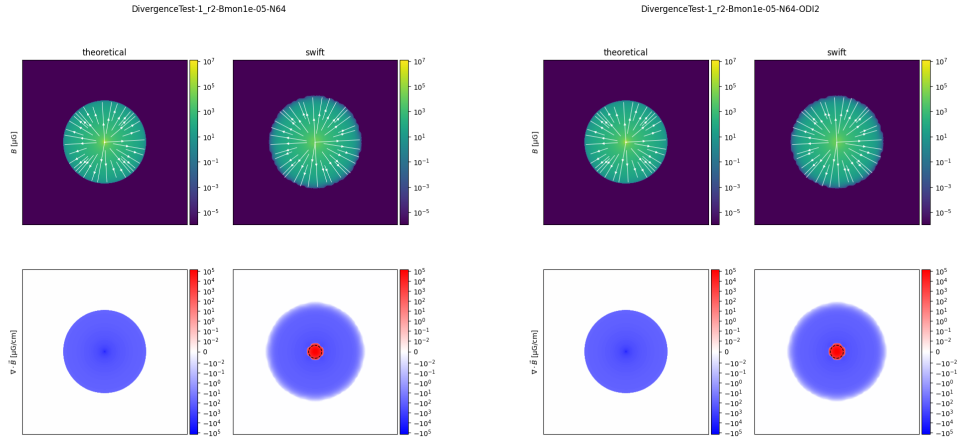

(a) anti-symmetric $\nabla \cdot \mathbf{B}$ operator (b) symmetric $\nabla \cdot \mathbf{B}$ operator

Figure 4.3: *The monopole field as computed by SWIFT for both the anti-symmetric (left) and the symmetric(right) divergence operator. For both figures the theoretical (left) and the SWIFT (right) fields have been plotted. The dashed circle in the SWIFT divergence field represents a circle with a radius of the compact support radius H around the monopole centre.*

4.2.1 Explanation SPH divergence operator erros

The question now is whether this is a bug in the code or if this is an effect of SPH operators. To answer that question, take a spherically symmetric vector field $\mathbf{A}$ that has a monotonically non-increasing magnitude over r. Examples are the monopole field from the section above, the electric monopole field $\mathbf{E} \propto (1/r^2)\hat{r}$, or a field $\mathbf{A} = (1 - (r/r_s))\hat{r}$ with $r < r_s$. Then, take the line $y = z = 0$ and look at the x-component of the field. Because of spherical symmetry it doesn't matter which line through the origin is taken. In the following derivation we will assume that $A > 0$ for $x > 0$, but if the sign is reversed, the same will hold, the divergence error will also just switch sign.

The kernel can be chosen but their general properties are the same. The kernel gradient is evaluated as

$$\nabla_i W_{ij} = \frac{\mathbf{x}_i - \mathbf{x}_j}{|\mathbf{x}_i - \mathbf{x}_j|} \partial_{r,i} W_{ij} \tag{4.14}$$

Now the exact values of the kernel gradients are not important for this derivation, but the sign of it is. Since $\partial_r W_{ij} \leq 0$, $\text{sgn}(\nabla_i W_{ij}) = -\text{sgn}(\mathbf{x}_i - \mathbf{x}_j)$. Or in our simplified case, $\text{sgn}(\nabla_i W_{ij}) = -\text{sgn}(x_i - x_j)$.

Anti-Symmetric Operator

Let us first look at the Anti-Symmetric divergence operator:

$$(\nabla \cdot \mathbf{A})_i = -\frac{f_{ij}}{\rho_i} \sum_j m_j (\mathbf{A}_i - \mathbf{A}_j) \cdot \nabla_i W_{ij} \tag{4.15}$$

In the rest of the derivation, the notation $(\nabla \cdot \mathbf{A})_{ij}$ will be used to denote the contributions of neighbour j to the divergence at particle i.

Now take particle a at $x = x_a > 0$ such that it has neighbours j at positions $x_j > 0 \; \forall \; j$. Consequently $A_a > 0$ and $A_j > 0$. The neighbours can be divided into two groups: $x_{j_1} < x_a$ and $x_{j_2} > x_a$.

- $x_{j_1} < x_a$:
  $A_{j_1} > A_a$ and $\text{sgn}(\nabla_a W_{aj_1}) = -\text{sgn}(x_i - x_{j_1}) = -1$
  Thus $(\nabla \cdot \mathbf{A})_{aj_1} < 0$

- $x_{j_2} > x_a$:
  $A_{j_2} < A_a$ and $\text{sgn}(\nabla_a W_{aj_2}) = -\text{sgn}(x_i - x_{j_2}) = +1$
  Thus $(\nabla \cdot \mathbf{A})_{aj_2} < 0$

Since all the contributions of the neighbours are negative, the resulting divergence $(\nabla \cdot \mathbf{A})_i < 0$ as expected.

Next, take particle b at $x = x_b > 0$, such that it has neighbours j for which $x_j < 0$. Its neighbours can be divided into three groups: the two groups described above ($x_{j_1} < x_b$ for $x_{j_1} > 0$ and $x_{j_2} > x_b$ for $x_{j_2} > 0$) and a third group $x_{j_3} < x_b$ for $x_{j_3} < 0$. For the third group:

- $x_{j_3} < 0 < x_b$:
  $A_{j_3} < 0$ such that $\text{sgn}(A_i - A_{j_3}) = +1$
  $\text{sgn}(\nabla_a W_{aj_3}) = -\text{sgn}(x_i - x_{j_3}) = -1$
  Thus $(\nabla \cdot \mathbf{A})_{bj_3} > 0$

Since this contribution is positive, this could lead to the total sum over the neighbours to end up positive, in contrast to the theoretical divergence.

Symmetric Operator

Let us now look at the symmetric divergence operator, and make the simplification that there are no large gradients in the smoothing lengths and density. Then $f_{ij} \sim 1$, $\rho_i \sim \rho_j \sim \rho$, $\nabla_i W_{ij} = \nabla_i W_{ji}$ and the operator is

given by:

$$(\nabla \cdot \mathbf{A})_i = -\rho_i \sum_j m_j \left[\frac{f_{ij}\mathbf{A}_i \cdot \nabla_i W_{ij}}{\rho_i^2} + \frac{f_{ji}\mathbf{A}_j \cdot \nabla_i W_{ji}}{\rho_j^2} \right] \tag{4.16}$$

$$\approx -\frac{1}{\rho} \sum_j m_j \left[\mathbf{A}_i + \mathbf{A}_j \right] \cdot \nabla_i W_{ij} \tag{4.17}$$

We will take the same approach as for the anti-symmetric operator, so let us start by taking a particle a at $x = x_a > 0$ such that it has neighbours j at positions $x_j > 0 \; \forall \; j$. Consequently $A_a > 0$ and $A_j > 0$. The neighbours can be divided into two groups: $x_{j_1} < x_a$ and $x_{j_2} > x_a$.

- $x_{j_1} < x_a$:
  $\text{sgn}(\nabla_a W_{aj_1}) = \text{sgn}(\nabla_a W_{j_1 a}) = -\text{sgn}(x_i - x_{j_1}) = -1$
  Thus $(\nabla \cdot \mathbf{A})_{aj_1} < 0$

- $x_{j_2} > x_a$:
  $\text{sgn}(\nabla_a W_{aj_2}) = \text{sgn}(\nabla_a W_{j_2 a}) = -\text{sgn}(x_i - x_{j_2}) = +1$
  Thus $(\nabla \cdot \mathbf{A})_{aj_2} > 0$

Now it is not immediately obvious that the result will be negative, but given that the field values for the first group are larger than for the second, $A_i + A_{j_1} > A_i + A_{j_2}$, the negative contributions will be larger than the positive ones and the divergence will result in a negative number.

Next, take particle b at $x = x_b > 0$, such that it has neighbours j for which $x_j < 0$. Its neighbours can be divided into four groups: the two groups described above ($x_{j_1} < x_b$ for $x_{j_1} > 0$ and $x_{j_2} > x_b$ for $x_{j_2} > 0$), a third group $x_{j_3} < 0 < x_b$ and $|x_{j_3}| < x_b$ and a fourth group $x_{j_4} < 0 < x_b$ and $|x_{j_4}| > x_b$. For the last two groups:

- $x_{j_3} < 0 < x_b$ and $|x_{j_3}| < x_b$:
  $|A_{j_3}| < 0$ and $|A_{j_3}| > A_b$, therefore $A_i + A_{j_3} < 0$
  $\text{sgn}(\nabla_a W_{aj}) = -\text{sgn}(x_i - x_j) = -1$
  Thus $(\nabla \cdot \mathbf{A})_{bj_3} > 0$

- $x_{j_4} < 0 < x_b$ and $|x_{j_4}| > x_b$:
  $|A_{j_4}| < 0$ and $|A_{j_4}| < A_b$, therefore $A_i + A_{j_4} > 0$
  $\text{sgn}(\nabla_a W_{aj}) = -\text{sgn}(x_i - x_j) = -1$
  Thus $(\nabla \cdot \mathbf{A})_{bj_4} < 0$

There is now an extra group of neighbours having positive contributions towards the total divergence. Since these neighbours would have

Version of March 12, 2025– Created March 12, 2025 - 17:00

been in group j_1 for particle a (having negative contributions), the positive contributions can now outweigh the negative contributions. There is an extra group j_4 also having negative contributions, but since $|A_{j_4}| < |A_{j_3}|$ these might not be enough.

Region of Error

The region where this divergence could be positive, is the region where a particle 'sees' neighbours at the opposite side of the monopole. In other words the distance of the particle to the monopole centre, should be smaller than the compact support radius $H = \gamma_K h$. The region where this holds is indicated in the figure 4.3 and it corresponds approximately to the region where the divergence is positive.

Remarks

This whole derivation was simplified by only looking at the x component of the divergence. However, the derivation is exactly the same for the y, and z components. And is therefore sufficient to conclude that there are positive contributions in the sum over neighbours that could 'erase' the correct negative contributions, leading to an incorrect positive divergence.

Also note that, while this derivation came from observations of errors in the magnetic field divergence, it holds for general fields with the conditions described above. This derivation should be seen more as a general explanation of why SPH divergences can be expected to diverge from the actual divergence.

While this derivation only shows, that the symmetric and anti-symmetric divergence operators could be wrong for these fields, it does not touch on the questions under what conditions they do so. That would require a more in depth analysis of the operators, including possibly particle arrangements, actual values of the kernel gradients and the vector field itself.

Lastly, it is up the the user of the operators to determine whether errors in the divergence estimate will lead to problems in their simulations or errors in their interpretations of them. The monopole from the example is unlikely to happen in real MHD simulations, however for other quantities they could be possible when including source terms of that quantity.

Chapter 5

Discussion

As we have seen in chapter 3, we have constructed a set of stable cosmological SPMHD simulations including subgrid models. With the inclusion of subgrid models, the SWIFT MHD branch is a first of a kind. All current SPMHD simulations have only included adiabatic physics. The mass resolutions of the simulations correspond to the low (our 128^3) and the intermediate (our 256^3) resolution FLAMINGO runs, but note that FLAMINGO's box size is much larger. (Schaye et al., 2023) Our 256^3 runs compare to the 256-runs of Marinacci et al. (2015) in terms of mass resolution, and our box sizes are comparable.

Next steps would be refining the stellar feedback model and including the last major subgrid model, black holes and AGN feedback. Also a resolution study could be done to see if we are resolving essential processes well.

One of the main problems that need addressing, is the instability when introducing resistivity, both physical and artificial. When introduced, they both caused large distortions of the velocity field and the (B, ρ) space. Nonetheless, these "ideal" MHD simulations are a good benchmark. Note that numerical simulations are seldom truly ideal, but always suffer from numerical diffusion due to the discretisation of your volume.

Another question is how the magnetic fields of gas particles should be treated when they are turned into stars, and the same will go when including black holes. The current implementation removes the gas particle and its magnetic field. This leads to a divergence, which is small enough to be cleaned by the Dedner cleaning. The reason it is done like this, is that it is not certain what exactly happens to the magnetic field when a star is formed and how it evolves after formation. However, it does not simply disappear. Thus it is certainly worth a thought how magnetic fields can be

incorporated into stars and black holes.

Even without the inclusion of resistivity, there is a large amount of questions that can be investigated. A set of possible correlations is presented in Marinacci et al. (2015), such as a relation between magnetic field and central temperature, or the relation between central magnetic field and halo mass. Also the effect of the subgrid models on the different regions (clusters, filaments, voids) could be investigated. We have also very briefly discussed the effects of changing the initial magnetic field, but that investigation can be expanded by for example examining the effect on different regions of the universe, or investigating the resulting magnetic power spectrum for different initial conditions.

Investigating the evolution of the magnetic field in voids of the universe would also be very interesting. Since the magnetic field there is below the current observation limit, the SWIFT code could provide meaningful predictions. One could investigate the magnetisation due to outflows or jets from high density regions and the effect different seeding mechanisms would have on the magnetic field. One note should be made that for a correct formulation of jets, resistivity should be included, which is as of now not stable.

We have briefly touched on the construction of simulated RM maps. Besides the already mentioned shortcomings of the assumed electron density and low amount of cluster samples, the study can also be extended to a deeper analysis of the RM distribution, its scatter profiles and overall deeper analysis of the profile shapes.

Chapter 6

Conclusion

In this research we have set up various cosmological box simulations using the MHD branch of the SWIFT SPH solver. We have varied subgrid models and operators for these simulations and studied the properties of the structure within. The presented simulations will be made publicly available. Our main results are as follows.

1. We have observed that using an anti-symmetric operator for the magnetic field divergence in the Dedner scalar field evolution leads to explosions in the simulations that include cooling, probably due to the high density contrasts caused by this process.

2. Using the symmetric operator however resulted in a set of stable cosmological SPMHD simulations, with only adiabatic physics, including cooling, or including cooling and stellar feedback. They were not stable when any kind of resistivity, was included.

3. The adiabatic simulations followed the theoretical adiabatic amplification relation nicely. The cooling and cooling+stellar feedback showed amplification to magnetic field values beyond adiabatic, $\sim 10^3$ µG and $\sim 10^2$ µG respectively.

4. While the two simulations including cooling extended to higher than observed magnetic fields, the one also including stellar feedback roughly corresponds to earlier simulations.

5. We have investigated the magnetic field profiles of the FoF groups and observed the formation of substructure in the halo profiles in the cooling simulation. We have observed central magnetic fields of

$\sim 10^{-2}$ μG, $\sim 10^{2}$ μG and ~ 10 μG for the adiabatic, cooling only and cooling+stellar feedback simulations respectively.

6. We have constructed simulated RM maps of the largest halo in the adiabatic, cooling, and cooling+stellar feedback simulations. While naively constructed, they roughly correspond to the literature, with $|\mathrm{RM}|$ reaching values of ~ 10 rad m^{-2} for the adiabatic simulation and $\sim 10^{3}$ rad m^{-2} for the cooling and cooling+stellar feedback simulations.

7. We have touched upon the possibilities of investigating effects of different initial magnetic field configurations.

8. We have discussed the shortcomings of SPH at density contrasts, and for large monopoles.

Acknowledgements

This research project made use of the SWIFT open-source simulation code (https://swift.strw.leidenuniv.nl/, Schaller et al. (2024, 2018)). Specifically the MHD branch was used, which will be released later. I thank the Leiden Observatory for letting me use their servers for the computational tasks. `Swiftsimio` was used to read and visualise the SWIFT outputs. (Borrow and Borrisov, 2020; Borrow and Kelly, 2021) The python libraries `numpy`, `matplotlib` and `scipy` were used to analyse and visualise the obtained data.

I would like to take this opportunity to thank my daily supervisor Nikyta Shchutskyi, for all his invaluable help during this project. I would like to thank my supervisor Matthieu Schaller for helping with the direction of this research project when I was stuck. Furthermore I would like to thank Orestis Karapiperis for helping me with questions about the SWIFT MHD code and giving me tips to improve the simulations, and Federico Stasyszyn for helping providing context with the produced results. I would also like to thank my friend and fellow Msc. student Simone van der Schot for all useful discussions about this research.

Bibliography

David J. Barnes, Daisuke Kawata, and Kinwah Wu. Cosmological simulations using GCMHD+. MNRAS, 420(4):3195–3212, March 2012. doi: 10.1111/j.1365-2966.2011.20247.x.

Josh Borrow and Alexei Borrisov. swiftsimio: A python library for reading swift data. *Journal of Open Source Software*, 5(52):2430, 2020. doi: 10.21105/joss.02430. URL https://doi.org/10.21105/joss.02430.

Josh Borrow and Ashley J. Kelly. Projecting sph particles in adaptive environments. 2021.

S. Børve, M. Omang, and J. Trulsen. Regularized Smoothed Particle Hydrodynamics: A New Approach to Simulating Magnetohydrodynamic Shocks. ApJ, 561(1):82–93, November 2001. doi: 10.1086/323228.

S. Børve, M. Omang, and J. Trulsen. Two-dimensional MHD Smoothed Particle Hydrodynamics Stability Analysis. ApJS, 153(2):447–462, August 2004. doi: 10.1086/421520.

Robert A. Crain, Joop Schaye, Richard G. Bower, Michelle Furlong, Matthieu Schaller, Tom Theuns, Claudio Dalla Vecchia, Carlos S. Frenk, Ian G. McCarthy, John C. Helly, Adrian Jenkins, Yetli M. Rosas-Guevara, Simon D. M. White, and James W. Trayford. The eagle simulations of galaxy formation: calibration of subgrid physics and model variations. *Monthly Notices of the Royal Astronomical Society*, 450(2):1937–1961, April 2015. ISSN 0035-8711. doi: 10.1093/mnras/stv725. URL http://dx.doi.org/10.1093/mnras/stv725.

A. Dedner, F. Kemm, D. Kröner, C. D. Munz, T. Schnitzer, and M. Wesenberg. Hyperbolic Divergence Cleaning for the MHD Equations.

Journal of Computational Physics, 175(2):645–673, January 2002. doi: 10.1006/jcph.2001.6961.

K. Dolag and F. Stasyszyn. An MHD GADGET for cosmological simulations. MNRAS, 398(4):1678–1697, October 2009. doi: 10.1111/j.1365-2966.2009.15181.x.

P. Domínguez-Fernández, F. Vazza, M. Brüggen, and G. Brunetti. Dynamical evolution of magnetic fields in the intracluster medium. MNRAS, 486(1):623–638, June 2019. doi: 10.1093/mnras/stz877.

J. Donnert, F. Vazza, M. Brüggen, and J. ZuHone. Magnetic Field Amplification in Galaxy Clusters and Its Simulation. Space Sci. Rev., 214(8):122, December 2018. doi: 10.1007/s11214-018-0556-8.

Y. Dubois and R. Teyssier. Cosmological MHD simulation of a cooling flow cluster. A&A, 482(2):L13–L16, May 2008. doi: 10.1051/0004-6361:200809513.

Pascal J. Elahi, Robert J. Thacker, and Lawrence M. Widrow. Peaks above the Maxwellian Sea: a new approach to finding substructures in N-body haloes. MNRAS, 418(1):320–335, November 2011. doi: 10.1111/j.1365-2966.2011.19485.x.

Pascal Jahan Elahi, Rhys Poulton, and Rodrigo Canas. VELOCIraptor-STF: Six-dimensional Friends-of-Friends phase space halo finder. Astrophysics Source Code Library, record ascl:1911.020, November 2019.

Sébastien Galtier. *Introduction to Modern Magnetohydrodynamics*, chapter I.2 - Magnetohydrodynamics, pages 19–31. Cambridge University Press, 2016.

F. Govoni, M. Murgia, V. Vacca, F. Loi, M. Girardi, F. Gastaldello, G. Giovannini, L. Feretti, R. Paladino, E. Carretti, R. Concu, A. Melis, S. Poppi, G. Valente, G. Bernardi, A. Bonafede, W. Boschin, M. Brienza, T. E. Clarke, S. Colafrancesco, F. de Gasperin, D. Eckert, T. A. Enßlin, C. Ferrari, L. Gregorini, M. Johnston-Hollitt, H. Junklewitz, E. Orrù, P. Parma, R. Perley, M. Rossetti, G. B Taylor, and F. Vazza. Sardinia Radio Telescope observations of Abell 194. The intra-cluster magnetic field power spectrum. A&A, 603:A122, July 2017. doi: 10.1051/0004-6361/201630349.

Federica Govoni and Luigina Feretti. Magnetic Fields in Clusters of Galaxies. *International Journal of Modern Physics D*, 13(8):1549–1594, January 2004. doi: 10.1142/S0218271804005080.

D. Guidetti, M. Murgia, F. Govoni, P. Parma, L. Gregorini, H. R. de Ruiter, R. A. Cameron, and R. Fanti. The intracluster magnetic field power spectrum in Abell 2382. A&A, 483(3):699–713, June 2008. doi: 10.1051/0004-6361:20078576.

D. Guidetti, R. A. Laing, M. Murgia, F. Govoni, L. Gregorini, and P. Parma. Structure of the magnetoionic medium around the Fanaroff-Riley Class I radio galaxy 3C 449. A&A, 514:A50, May 2010. doi: 10.1051/0004-6361/200913872.

Kazunari Iwasaki. Minimizing dispersive errors in smoothed particle magnetohydrodynamics for strongly magnetized medium. *Journal of Computational Physics*, 302:359–373, December 2015. doi: 10.1016/j.jcp.2015.09.022.

Russell M. Kulsrud. *Plasma Physics for Astrophysics*. 2004.

Federico Marinacci, Mark Vogelsberger, Philip Mocz, and Rüdiger Pakmor. The large-scale properties of simulated cosmological magnetic fields. MNRAS, 453(4):3999–4019, November 2015. doi: 10.1093/mnras/stv1692.

Salome Mtchedlidze, Paola Domínguez-Fernández, Xiaolong Du, Axel Brandenburg, Tina Kahniashvili, Shane O'Sullivan, Wolfram Schmidt, and Marcus Brüggen. Evolution of Primordial Magnetic Fields during Large-scale Structure Formation. ApJ, 929(2):127, April 2022. doi: 10.3847/1538-4357/ac5960.

Andrii Neronov and Ievgen Vovk. Evidence for Strong Extragalactic Magnetic Fields from Fermi Observations of TeV Blazars. *Science*, 328(5974):73, April 2010. doi: 10.1126/science.1184192.

E. Osinga, R. J. van Weeren, F. Andrade-Santos, L. Rudnick, A. Bonafede, T. Clarke, K. Duncan, S. Giacintucci, T. Mroczkowski, and H. J. A. Röttgering. The detection of cluster magnetic fields via radio source depolarisation. A&A, 665:A71, September 2022. doi: 10.1051/0004-6361/202243526.

E. Osinga, R. J. van Weeren, L. Rudnick, F. Andrade-Santos, A. Bonafede, T. Clarke, K. Duncan, S. Giacintucci, and H. J. A. Röttgering. Probing

cluster magnetism with embedded and background radio sources in Planck clusters. A&A, 694:A44, February 2025. doi: 10.1051/0004-6361/202451885.

G. J. Phillips and J. J. Monaghan. A numerical method for three-dimensional simulations of collapsing, isothermal, magnetic gas clouds. MNRAS, 216:883–895, October 1985. doi: 10.1093/mnras/216.4.883.

Kenneth G. Powell, Philip L. Roe, Timur J. Linde, Tamas I. Gombosi, and Darren L. De Zeeuw. A Solution-Adaptive Upwind Scheme for Ideal Magnetohydrodynamics. *Journal of Computational Physics*, 154(2):284–309, September 1999. doi: 10.1006/jcph.1999.6299.

D. J. Price and J. J. Monaghan. Smoothed Particle Magnetohydrodynamics - III. Multidimensional tests and the ∇.B= 0 constraint. MNRAS, 364(2): 384–406, December 2005. doi: 10.1111/j.1365-2966.2005.09576.x.

Daniel J. Price. Smoothed particle hydrodynamics and magnetohydrodynamics. *Journal of Computational Physics*, 231(3):759–794, February 2012. doi: 10.1016/j.jcp.2010.12.011.

Daniel J. Price, James Wurster, Terrence S. Tricco, Chris Nixon, Stéven Toupin, Alex Pettitt, Conrad Chan, Daniel Mentiplay, Guillaume Laibe, Simon Glover, Clare Dobbs, Rebecca Nealon, David Liptai, Hauke Worpel, Clément Bonnerot, Giovanni Dipierro, Giulia Ballabio, Enrico Ragusa, Christoph Federrath, Roberto Iaconi, Thomas Reichardt, Duncan Forgan, Mark Hutchison, Thomas Constantino, Ben Ayliffe, Kieran Hirsh, and Giuseppe Lodato. Phantom: A Smoothed Particle Hydrodynamics and Magnetohydrodynamics Code for Astrophysics. PASA, 35: e031, September 2018. doi: 10.1017/pasa.2018.25.

M. S. Pshirkov, P. G. Tinyakov, and F. R. Urban. New Limits on Extragalactic Magnetic Fields from Rotation Measures. Phys. Rev. Lett., 116 (19):191302, May 2016. doi: 10.1103/PhysRevLett.116.191302.

L. Rudnick and F. N. Owen. The distribution of polarized radio sources ¿15 ÎŒjy in goods-n. *The Astrophysical Journal*, 785(1):45, mar 2014. doi: 10.1088/0004-637X/785/1/45. URL `https://dx.doi.org/10.1088/0004-637X/785/1/45`.

Matthieu Schaller et al. SWIFT: SPH With Inter-dependent Fine-grained Tasking. Astrophysics Source Code Library, May 2018.

Matthieu Schaller et al. SWIFT: A modern highly-parallel gravity and smoothed particle hydrodynamics solver for astrophysical and cosmological applications. MNRAS, 530(2):2378–2419, May 2024. doi: 10.1093/mnras/stae922.

Joop Schaye, Robert A. Crain, Richard G. Bower, Michelle Furlong, Matthieu Schaller, Tom Theuns, Claudio Dalla Vecchia, Carlos S. Frenk, I. G. McCarthy, John C. Helly, Adrian Jenkins, Y. M. Rosas-Guevara, Simon D. M. White, Maarten Baes, C. M. Booth, Peter Camps, Julio F. Navarro, Yan Qu, Alireza Rahmati, Till Sawala, Peter A. Thomas, and James Trayford. The EAGLE project: simulating the evolution and assembly of galaxies and their environments. MNRAS, 446(1):521–554, January 2015. doi: 10.1093/mnras/stu2058.

Joop Schaye, Roi Kugel, Matthieu Schaller, John C. Helly, Joey Braspenning, Willem Elbers, Ian G. McCarthy, Marcel P. van Daalen, Bert Vandenbroucke, Carlos S. Frenk, Juliana Kwan, Jaime Salcido, Yannick M. Bahé, Josh Borrow, Evgenii Chaikin, Oliver Hahn, Filip Huško, Adrian Jenkins, Cedric G. Lacey, and Folkert S. J. Nobels. The FLAMINGO project: cosmological hydrodynamical simulations for large-scale structure and galaxy cluster surveys. MNRAS, 526(4):4978–5020, December 2023. doi: 10.1093/mnras/stad2419.

Kandaswamy Subramanian. The origin, evolution and signatures of primordial magnetic fields. *Reports on Progress in Physics*, 79(7):076901, July 2016. doi: 10.1088/0034-4885/79/7/076901.

G. B. Taylor, A. C. Fabian, and S. W. Allen. Magnetic fields in the Centaurus cluster. MNRAS, 334(4):769–776, August 2002. doi: 10.1046/j.1365-8711.2002.05555.x.

Terrence S. Tricco and Daniel J. Price. Constrained hyperbolic divergence cleaning for smoothed particle magnetohydrodynamics. *Journal of Computational Physics*, 231(21):7214–7236, August 2012. doi: 10.1016/j.jcp.2012.06.039.

Terrence S. Tricco, Daniel J. Price, and Matthew R. Bate. Constrained hyperbolic divergence cleaning in smoothed particle magnetohydrodynamics with variable cleaning speeds. *Journal of Computational Physics*, 322:326–344, October 2016. doi: 10.1016/j.jcp.2016.06.053.

Robert P. C. Wiersma, Joop Schaye, and Britton D. Smith. The effect of photoionization on the cooling rates of enriched, astrophysical plasmas.

MNRAS, 393(1):99–107, February 2009. doi: 10.1111/j.1365-2966.2008.14191.x.